# Electrical transport properties of nitrogen doped carbon microspheres

**William Patrick Wright**

A dissertation submitted to the Faculty of Science, University of the Witwatersrand, Johannesburg, in fulfilment of the requirements for the degree of Master of Science.

School of Physics

University of the Witwatersrand

October 2013

# Declaration

I declare that this dissertation is my own, unaided work, other than where specifically acknowledged. It is being submitted in fulfilment of the requirements for the degree of Master of Science to the University of the Witwatersrand, Johannesburg. It has not been previously submitted for any degree or examination in any other university.

Signed this 9th day of April 2014

William Patrick Wright

# Abstract

A suite of four samples of nitrogen doped carbon microspheres, each with a different level of nitrogen dopant, was synthesised in a horizontal chemical vapour deposition reaction. The samples were characterized using scanning electron microscopy, Raman spectroscopy and electron paramagnetic resonance spectroscopy. Scanning electron microscopy showed that microspheres were produced by the reaction. Raman spectroscopy confirmed the graphitic nature of the samples. Electron paramagnetic resonance spectroscopy determined that nitrogen was present in the graphitic lattice and was used as a non-destructive technique to measure the amount of substitutional nitrogen present in the samples. In order to perform electrical transport measurements an automated magneto-transport measurement station was developed in the laboratory. This transport station was computer controlled and contained all of the necessary hardware and software required to perform magneto-electrical transport measurements. Variable temperature electrical transport measurements were performed on all samples to determine their conductive properties. Resistance measurements showed that two of the samples were semiconductors while the other two samples displayed a transition to metallic behaviour at higher temperatures. This transition can be ascribed to the thermal desorption of nitrogen dopant. Models were fitted to the data and the semiconducting behaviour is best explained by a model of fluctuation induced tunnelling while the metallic behaviour is best explained by a quasi-1 dimensional metallic term based on electron-phonon interactions. The IV characteristics of two of the samples display increasing non-linearity of the current's voltage dependence with decreasing temperature. The other two samples exhibit this behaviour at lower temperatures while higher temperature IV data displays a current saturation with increasing voltage. The same models used to explain the resistance measurements can be used to explain the IV characteristics data extremely well. The magnetoresistance data taken with the direction of current flow orientated both parallel and perpendicular to the field, show a transition from negative to positive magnetoresistance with decreasing temperature. The results of these experiments are inconclusive, as a theoretical model of magnetoresistance in systems that conduct via fluctuation induced tunnelling is not well defined. A comparison between the resistance measurements of all four samples was made to determine the effect of nitrogen doping on the samples'

electronic transport properties. The result of this comparison was indeterminate. This was due to samples with identical nitrogen dopant levels displaying vastly different conductive properties and indicates that very strict synthesis conditions need to be adhered to in order to ensure sample quality. Resistance measurements were rerun on the two samples that displayed purely semiconducting behaviour to investigate the possibility of atmospheric doping. It was found that the samples now displayed a transition to metallic behaviour and a reduced resistance. These results are suggestive of atmospheric doping by oxygen and water vapour.

# Acronyms and Page Numbers

In this section, a list of commonly used acronyms in the text is presented. The meaning of each acronym is given followed by the number of the page of its first use.

**CMS** - carbon microsphere - 1

**CNF** - carbon nanofiber - 1

**CNH** - carbon nanohorn - 1

**CNS** - carbon nanosphere - 4

**CNT** - carbon nanotube - 1

**CVD** - chemical vapour deposition - 5

**CS** - carbon sphere - 2

**DAC** - digital to analogue converter - 33

**EELS** - electron energy loss spectroscopy - 10

**EPR** - electron paramagnetic resonance - 10

**ES-VRH** - Efros-Schklovski variable range hopping - 20

**FIT** - fluctuation induced tunnelling - 16

**FTIR** - Fourier transform infra-red - 10

**h-CVD** - horizontal chemical vapour deposition - 23

**n-CMS** - nitrogen doped carbon microsphere - 2

**SEM** - scanning electron microscopy - 9

**VRH** - variable range hopping - 15

**XPS** - X-ray photoelectron spectroscopy - 10

# Acknowledgements

I would like to thank my friends and family for all their love, care and support throughout the duration of this project. Without your encouragement I would not be where I am now. I would like to thank my supervisor Prof Jonathan M. Keartland for giving me the opportunity to undertake this research. Your guidance and mentoring was invaluable. I would like to thank Ross McIntosh for his help and useful discussions regarding electrical transport in carbon nanomaterials and general practices in performing transport experiments. Finally I would like to thank Vincent Marsicano for his invaluable assistance with the experimental components related to this research and for the late night discussions and ponderings in the laboratory.

The financial assistance of the National Research Foundation (NRF) towards this research is hereby acknowledged. Opinions expressed and conclusions arrived at, are those of the author and are not necessarily to be attributed to the NRF.

A conference proceedings publication and a peer reviewed journal article resulted from the work described in this dissertation:

'The electrical transport properties of bulk nitrogen doped carbon microspheres' by W. P. Wright, V. D. Marsicano, J. M. Keartland, R. M. Erasmus, S. Dube and N. J. Coville, Proceedings of the South African Institute of Physics Conference 2013, Currently Under Review.

'The electrical transport properties of nitrogen doped carbon microspheres' by W. P. Wright, V. D. Marsicano, J. M. Keartland, R. M. Erasmus, S. Dube and N. J. Coville, Materials Chemistry and Physics, Currently Under Review.

# Contents

# List of Figures

# List of Tables

# 1 Introduction

This chapter will serve as a preamble for this dissertation and will introduce the motivations and justifications for the research conducted. The aims of this research will be presented and discussed. Finally, the structure of the dissertation will be provided.

## 1.1 Motivation

Since the initial report on carbon nanotubes (CNTs) by Iijima in 1991 [10] and the limits of current semiconductor technology rapidly being reached, the scientific community is looking to smaller and smaller structures for the next generation of electronic devices. A vast number of different nanomaterials are currently being studied with the hope that they will one day allow for faster computation and possibly even lead to the invention of new devices.

Carbon nanomaterials have been of particular interest due to the fascinating properties that have been uncovered and the many different forms carbon nanomaterials can take. These include but are not limited to CNTs, carbon nanohorns (CNHs) and carbon nanofibers (CNFs). Some of these carbon allotropes such as CNTs have been intensly studied with thousands of papers being published every year on their physical and chemical properties as well as new and exciting applications. Others such as carbon microspheres (CMSs) are not nearly as well understood.

While spherical carbons such as carbon blacks have been studied and applied for many decades, the slightly larger CMSs this research is concerned with have only received attention more recently. This is in no small part due to the many novel properties already discovered and the interesting applications these properties have lead to. These include great physical strength, which has lead to their use as a strengthening additive, and dangling bonds present at the surface of CMSs. These dangling bonds are sites for functionalization which promises application in catalysis and lithium ion battery construction.

While these discoveries are exciting, there is still much to learn about these novel nanomaterials. Uncovering more of their physical properties will not only provide a greater academic understanding of CMSs, but will also allow for better use in their current applications and lead to new applications in the future.

The focus of this research will be on the electrical transport properties of nitrogen doped CMSs (n-CMSs). This is due to the fact that while conductivity measurements have been performed on pristine and boron doped samples of CMSs, the effect of nitrogen doping on electrical transport is still unknown. Knowledge of this will provide insight into the viability of using CMSs in next generation electronic devices.

## 1.2 Aims

The main aim of this research would be to gain a greater understanding of the electrical transport properties of n-CMSs. This will be achieved through performing a series of electrical transport measurements including resistance measurements, IV characteristics measurements and magnetoresistance measurements. In order to conduct these experiments, the required experimental setup will need to be developed. The influence of nitrogen doping effects on these measurements will be of particular interest. Performing variable temperature resistance measurements and variable temperature IV characteristics experiments will provide insight into the conduction mechanisms governing electrical transport while magnetoresistance measurements will provide information regarding any changes in conduction under the influence of magnetic fields. These results are important for determining the suitability of these materials for use in electronic devices. For example the experiments can show if the samples are metallic or semiconducting and whether doping improves conductivity.

## 1.3 Structure of Dissertation

Chapter 1 serves as an introduction to the dissertation and provides the aims of and motivation for the research contained in the dissertation. It also contains this description of the structure and organization of the chapters to follow.

Chapter 2 contains a literature review of the current state of research into CMSs. Information regarding synthesis techniques, physical and chemical properties and uses of CMSs

in technology and science is given. An overview of the current state of electrical transport in carbon spheres (CSs) is provided. This chapter also contains an overview of the transport properties of CNTs as some of the transport properties of CMSs are expected to be similar. A brief discussion of common transport mechanisms is also provided.

Chapter 3 contains information on the synthesis of the samples used in this research and the characterization experiments performed on them. A brief discussion of each of the techniques used and experiments performed is given and the results of the experiments are presented.

Chapter 4 gives the experimental procedure for the electrical transport experiments performed for this dissertation. A description of the experimental apparatus, required for all experiments as well as the sample preparation procedure and the process of taking readings in each case is provided. These sections include discussions on the software written and apparatus built to automate experiments.

Chapter 5 provides the results of the experiments performed and analysis of these results. Models are fitted to the obtained data and trends in the results are accounted for.

Chapter 6 gives the conclusions that can be drawn from this research. Suggestions for further work that can be performed to supplement this work are given.

The appendices contain supplementary information on the computer software written to automate the experiments.

# 2 Literature Review

The topic of carbon nanomaterials has rapidly become a vast area of scientific interest. Thousands of scientific papers have been published on their fundamental physical and chemical properties as well as their applications in areas as diverse as engineering and medicine. This chapter will provide an overview of the currently known properties and applications of carbon nanospheres (CNSs). It will also include a discussion of the electrical transport studies done on CNTs. These discussions provide a good basis for transport studies of carbon nanomaterials in general, as CNTs are by far the most studied and display interesting electrical transport properties. This discussion will be followed by a review of the transport studies performed on CNSs, as they are the focus of this research. Finally the chapter will conclude with a study of some of the theoretical transport models commonly applied to bulk samples of carbon nanomaterials.

## 2.1 Carbon Nanospheres

Since the discovery of Buckminsterfullerenes in the 1980's [11], interest in shaped carbon materials and nanomaterials in particular has sky rocketed. Some of the shaped carbon materials that have been discovered since then include CNTs [10], CNFs [12], CNHs [13] and CNSs [14]. By far the most intensely studied of these has been CNTs due to their novel physical [15] and chemical [16] properties and many possible applications [17]. In light of this interest in nanomaterials, attention has been refocused on the historically significant spherically shaped carbon materials. These materials have found use as strengthening additives [18], pigments in inks (as seen in the patent by Belmont *et al*) [19] and as cathodes in batteries [20]. The use of spheres as a strengthening additive has been further confirmed by studying their great mechanical strength [21].

Spherical carbon materials have a variety of sizes and types and as a result have been given a variety of names. Some of these include CNSs, carbon blacks, carbon microbeads, mesoporous microbeads and onions [1]. The spherical shape of these materials is taken up as a result of energy minimization and occurs during synthesis [22]. A number of different

classification systems have been developed to try and differentiate between them based on their nanometric texture [23] and size [24]. Unlike Buckminsterfullerenes which consist of a set number of carbon atoms, CSs generally consist of flakes of graphite that are either arranged in concentric layers which are perpendicular to the radius of the sphere or are parallel to the radius of the sphere [23]. Figure 2.1 shows these different arrangements of graphite. Spheres can also vary greatly in size, ranging from a few nanometres in the case of Buckminsterfullerenes to microns in size. The size of the spheres being studied is largely dependent on the synthesis parameters. The spheres are attracted to one another by Van der Waals forces and form long chains and agglomerates. The spheres also have a tendency to occasionally accrete during the synthesis process. This is typically found in chemical vapour deposition (CVD) synthesis processes. Spheres are also found to be hollow or solid (the core consists of graphite flakes). Hollow spheres can be created in a number of different ways, the most common being templating. In this process carbon is allowed to arrange itself on the surface of a spherical molecule such as a metal. This has the benefit of imparting the resulting CS with the novel properties of the template [25]. The template can also be removed at a later stage via a thermal process leaving a hollow CS.

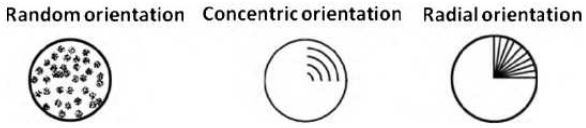


Figure 2.1: A simple diagram demonstrating how graphite layers can be arranged in different ways to form carbon spheres [1]

### 2.1.1 Formation and Structure

A number of different mechanisms have been proposed to explain the growth of CSs. Each of these mechanisms can be dependent on varied factors that define the synthesis process. A number of mechanisms have been proposed that deal with a specific synthesis process. However the dominant factor is the presence of a catalyst or a template in the reaction. Only the most general mechanisms for sphere formation will be considered here.

Soot from combustion is an intensely studied form of carbon that is generally spherical in nature. It is believed that the formation of CSs in the gaseous phase bares many similarities with the formation of soot particles [26]. Many attempts have been made to study the formation process of carbon particles larger than soot or carbon black and it has been found that during dehydrogenation in pyrolysis reactions, polyaromatic hydrocarbons grow and, in time, the properties of smaller particles like carbon blacks develop [1].

The mechanism of larger sphere growth is still unknown but models have been proposed. One such model uses the nucleation of pentagonal rings of carbon atoms. These elements then combine resulting in spiral shell growth [11]. Figure 2.2 provides a diagrammatic representation of this process.

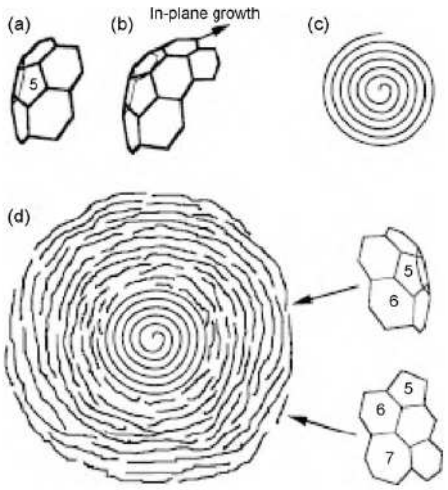


Figure 2.2: A diagrammatic depiction of the spiral shell formation from nucleated pentagonal rings. a) Pentagon nucleation b) quasi-icosahedral shell growth c) spiral shell formation d) formation of a larger sphere. [2]

Depending on their size, the surface structure of CSs has been observed to vary. In the case of smaller spheres, the surface can consist of an unbroken, curved sheet of carbon atoms. In larger spheres, typically diameters greater than 10nm, the spheres are observed to consist of flakes of graphite layered together. These flakes do not form closed spheres but do allow for the curvature of the sphere. In order for this curvature to be achieved, the inclusion of pentagonal, hexagonal and heptagonal rings of carbon is required [27]. The curvature of different carbon rings is shown in Figure 2.3. The edges of the these flakes are the source of the many dangling bonds which are sites for chemical activity [3]. The additional layers of carbon that make up the shells of the sphere are formed from the deposition of gaseous phase carbon. The mechanism behind the formation of spheres where the carbon layers are perpendicular to the central core is still unknown and further studies are required to shed light on this topic.

The inclusion of a catalyst in the synthesis process influences the formation of CSs in a subtle way. Metal nanoparticle templates can be used to create hollow CSs by allowing the carbon matrix to form around the template and then removing the template post synthesis. However catalysts can also be used to manufacture solid spheres which suggest that in these reactions, the catalysts aid in the decomposition of the carbon containing precursor. It is believed that the inclusion of a metal catalyst to produce solid spheres

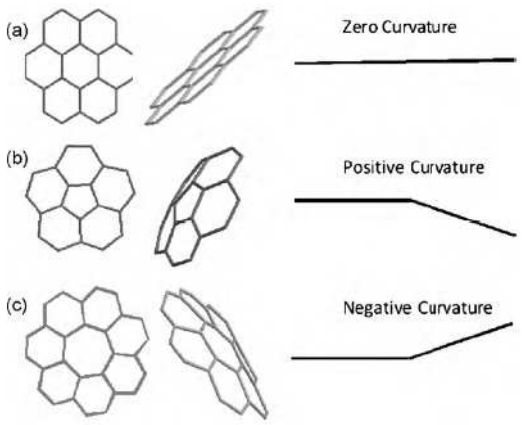


Figure 2.3: A diagrammatic representation of a) Hexagonal, b) Pentagonal and c) Heptagonal carbon rings and how they affect the curvature of carbon flakes. [3]

has a similar effect to metal catalysis in the production of CNTs. In these situations, carbon is deposited on the surface of the metal template and dissolves in the metal. The carbon then precipitates into graphitic carbon. The carbon flakes may also be formed via the diffusion of carbon over the surface of the metal nanoparticle. The temperature of the reactor is an important factor in determining whether this mechanism acts to form CNTs or CSs [1].

### 2.1.2 Synthesis

Many techniques currently exist to successfully synthesize CNTs. This experience has lead to a similar plethora of synthesis methods for CS production. In addition spheres were often found as a by-product of the synthesis of CNTs. In order for spheres to be predominantly produced using techniques used for CNT production, the synthesis parameters have to be optimized to promote sphere growth. The methods used to synthesize CSs include: the arc discharge method, the laser ablation method, CVD and autoclave methods. There are many other techniques that include both catalytic and non-catalytic methods, but the above techniques are the most popular.

The arc discharge method uses an electrical discharge between two high purity graphite electrodes to cause the anode to sublimate and different shaped carbon materials to form at the cathode. This was the original method used to synthesize CNTs in bulk [28]. A number of different parameters affect the type and size of materials produced, including temperature of the reactor, electrode material and the atmosphere in which the reaction takes place. This method can produce both solid [29] and hollow spheres [30].Figure 2.4

shows a schematic diagram of a typical reactor used in arc discharge experiments.

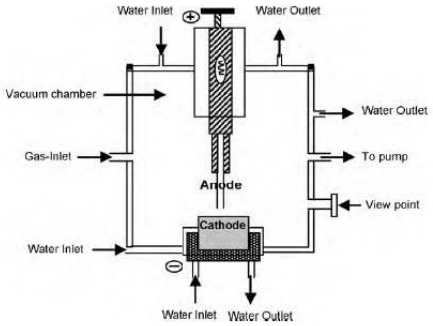


Figure 2.4: A schematic diagram of a typical arc discharge reactor [4]

Laser Ablation is a process in which a high powered laser is used to vapourize a carbon target (typically graphite). The system is placed inside a high temperature furnace and a carrier gas is fed into the system. The carrier gas transports the vapourized carbon to cooler parts of the reactor where the carbon condenses to form carbon nanomaterials. Water cooling of these surfaces is sometimes used to create a well-defined area where reaction products will form. Alterations to this technique can be made to enable the production of hollow CSs [31].

CVD is one of the most common synthesis techniques for producing carbon nanomaterials. Samples can be synthesised either with or without the use of a catalyst. Aside from this there are many ways in which the technique can be expanded upon to produce a wide variety of different materials, but the basic principle behind the technique remains the same: a gaseous or vapour precursor (often volatile) is converted to a solid product. This method will be treated in more detail in a subsequent chapter, but many examples of its usage can be found in the literature [32], [33]. Figure 2.5 shows the different kinds of hollow CSs that can be produced using CVD reactions.

The use of autoclaves to reduce the high temperature requirements for CS synthesis has been previously reported on [34]. Lower temperature synthesis is supplemented with a high pressure environment to achieve the desired products. A low temperature synthesis environment allows for a broader range of applications, particularly in electronics as high temperatures can destroy other materials in the electrical components. Great care must be taken to ensure that the materials the autoclave is constructed from do not interfere with the reaction or the products [35]. Autoclave methods also have the advantage of being able to work either with or without a catalyst.

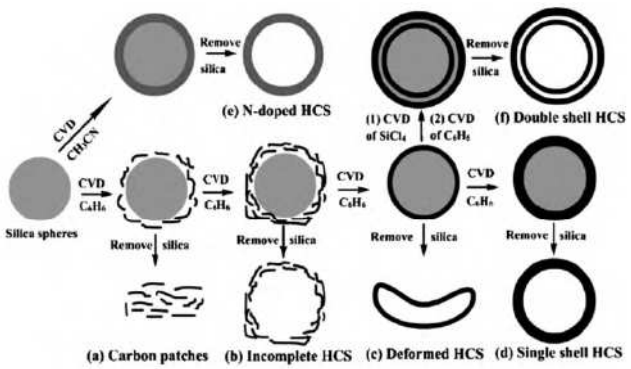


Figure 2.5: A diagram depicting the different kinds of hollow carbon spheres that can be produced from a chemical vapour deposition reactor. [5]

### 2.1.3 Chemical and Physical Properties

The chemical and physical properties of the vast family of CSs is of particular interest as knowledge of these properties will not only provide a greater academic understanding of these novel materials, but it will allow for their more effective use in their current applications, and hopefully shed light on new possible applications.

In order to achieve the curved shape of a sphere, the graphite flakes must consist of pentagonal and heptagonal rings of carbon atoms. This already indicates the chemistry of CSs will be different from graphite or CNTs as they consist primarily of hexagonal carbon rings. Another very important feature that affects the chemistry of CSs in general is the presence of dangling bonds on the surface. These dangling bonds provide sites for functionalization by organic molecules such as OH or COOH molecules. Functionalization allows for the modification of the properties of the CSs [36]. These functional groups can be added during the synthesis process or via post synthesis chemical treatment by acids and bases. Another important way in which the chemistry of CSs can be modified is via doping. Carbon atoms can be replaced with other atoms in the carbon matrix which alters the physical and chemical properties of the spheres. Typical elements that are used as dopants are nitrogen and boron [7], [37].

In order to study the physical properties of CSs, a number of different experiments can be performed. Electron microscopy, including scanning electron microscopy (SEM) and transmission electron microscopy (TEM), can be performed to study the morphology and composition of samples [21]. Electron microscopy will be dealt with in more detail in a subsequent chapter. X-ray diffraction is used as a non-destructive technique to study the crystallinity, purity and strain of samples. The crystallinity of a sample can be determined from the (002) diffraction peak at a scattering angle of $2\theta = 26.2^\circ$ [38].

Raman spectroscopy is a very well established characterization technique that can provide information regarding the structural and chemical properties of a sample. Like XRD, it can be used to determine the crystalinity of a sample. Raman spectroscopy will be dealt with in more detail in a subsequent chapter. Fourier transform infra-red (FTIR) spectroscopy is used to provide more in depth information on the chemical composition of a sample. Important bands for CSs seen in spectra obtained from FTIR spectroscopy are the 1630 $cm^{-1}$ band and the 2850-2920 $cm^{-1}$ band. Different functional groups present in a sample can also be observed using FTIR spectroscopy [1]. Further studies on the surface characteristics of CSs have been performed using mass spectrometry [39]. The chemical and thermal properties of samples can be studied using thermogravimetric analysis [40]. Electron paramagnetic resonance (EPR) spectroscopy has been used as a technique to probe the magnetic properties of CSs [41]. EPR spectroscopy will be dealt with in more detail in a subsequent chapter. X-ray photoelectron spectroscopy (XPS) has been used as a technique to further probe the chemical environment of CSs, particularly with regard to carbon and dopant atoms. A C1 peak has been found in XPS spectra at 284 eV [42]. This peak indicates the presence of carbon 1s electrons and a high resolution spectra of this peak provides information on other carbon bonds. Electron energy loss spectroscopy (EELS) is used to determine the level of graphitization of the CSs. A sharp peak is found at 285 eV. This provides information regarding the structural quality of the sample [43]. Classical strength measurements have been performed on CS samples and it has been found that they possess great physical strength with failure under a compressive load occurring at 830±69 MPa and the tensile strength estimated to be 8.3±0.69 GPa [1].

### 2.1.4 Applications

The unique properties of spherical carbon materials such as carbon black have been exploited in novel applications for many years. However the discovery of these newer types of spherical carbons has led to new applications ranging from strengthening additives to anode materials in lithium ion batteries, with many potential uses on the horizon. Some of the current uses will now be discussed.

CSs have become favourite candidates for use in fuel cells, batteries and electrical components such as capacitors. Mesocarbon microbeads were included as electrodes in both lithium and sodium batteries and after heat treatment of the spheres greatly improved electrical characteristics were obtained[44]. These studies have been supplemented with work studying the effect of annealing on the discharge behaviour of CSs intercalated with lithium ions [45]. For applications in direct methanol fuel cells, CSs are used for electrocatalysis with platinum and ruthenium [46]. Both hollow CSs and mesocarbon

microbeads have been used to overcome porosity problems associated with the usage of carbon black [47]. Doped CSs have found use in semiconductor electronics. For example nitrogen enriched CSs have found use in electrochemical capacitors [48].

Field emission is an important physical property that is desirable for fields such as vacuum electronics. These devices find use in space propulsion systems and scientific equipment. Previously metallic emitters were used, but carbon is an attractive alternative. This is due to the fact that carbon is one of the best known cold emitters of electrons and the potential cost saving using carbon offers. Intense research is being applied to using carbon nanomaterials as field emitters [49].

The vast physical strength of carbon materials such as diamond and CNTs suggests the possible usage of other carbon allotropes as a strong material. Carbon blacks have long found usage as a strengthening additive to rubber and rubberized compounds and other kinds of CSs are being used for similar applications [50]. As an additive, CSs have found usage in lubricants and recently have been applied in shock wave protection materials and sealants [51].

An important potential use of CSs is in chemistry as a catalyst and catalyst support[52]. Their use as a catalyst is due to the presence of dangling bonds on the surface of the sphere which are active sites for chemistry. CSs offer many advantages as a catalyst over other carbon allotropes such as CNTs. They can be easily synthesised with high purity and their physical properties can be finely tuned. Currently the primary use of CSs in catalysis is as a support for metal nanoparticles such as lead [53] and palladium [54].

CSs have found use as a component in composite materials. This allows for the modification of the physical and chemical properties of the composite [55]. The addition of CSs to a composite can be achieved via simple mixing or via chemical reaction. Surface modification of the CSs can ease the chemical binding between the CSs and composite.

Some more novel uses of CSs have also been identified that are environmental in essence. CSs acting as supports for lead nanoparticles have been used to slow down the ripening of fruits and vegetables in storage via the removal of ethylene [56]. Carbon blacks have also been shown to extract the organic pollutants from water [1].

## 2.2 Electrical Transport in Carbon Nanotubes

In this section the electrical transport properties of CNTs will be reviewed. This is useful as the transport properties of CSs are not nearly as well studied or understood and the transport properties of CNTs will provide a good starting point when attempting to model the transport behaviour of CSs. The novel transport phenomena observed in CNTs are also of interest as they will provide a reference point should similar behaviour be seen in CSs. A brief discussion of the structure of single walled CNTs will be given. This is due to the transport properties of CNTs being intrinsically linked to their physical structure. A review of some of the transport phenomena observed in both individual and bulk CNTs will be provided. The focus will be on experimental results with mention given to theoretical models were applicable. Emphasis will be placed on results related to the experiments conducted in this research.

### 2.2.1 Structure of Carbon Nanotubes

A single walled CNT consists of a single sheet of graphene that has been rolled into a tube. Graphene is a 2-dimensional sheet of carbon atoms arranged into a honeycomb lattice. How the sheet is rolled up is determined by a vector known as the chiral vector. The chiral vector is constructed using the unit vectors of the 2 dimensional graphene sheet and is given by:

$$C_h = ma_1 + na_2 \tag{2.1}$$

where $a_1$ and $a_2$ are the unit vectors of the graphene sheet and $m$ and $n$ are integers. Different values of $m$ and $n$ lead to different kinds of tubes being formed, namely chiral tubes and non-chiral tubes. This is because the point $(m, n)$ represents a point on the graphene lattice and the chiral vector will join the origin and this point. The chiral vector also determines the diameter of the CNT. The diameter of a CNT is given by:

$$d = \frac{a\sqrt{m^2 + mn + n^2}}{\pi} \tag{2.2}$$

where $a$ is the lattice constant for graphene. Figure 2.6 shows how one can construct a (5,3) CNT by rolling up a graphene sheet using the chiral vector. The chiral angle is another important quantity that can be defined. It is defined as being the angle between

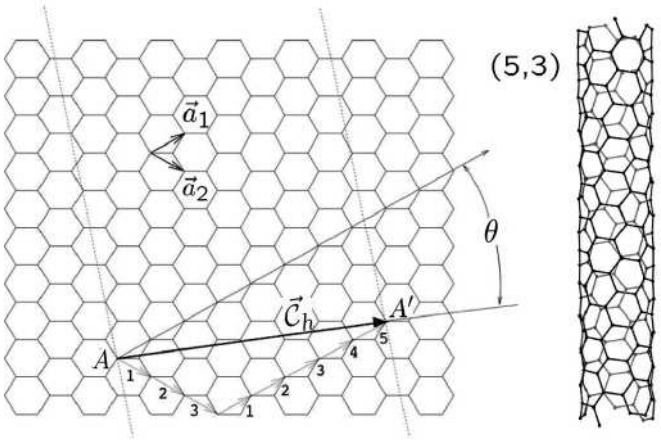


Figure 2.6: A diagram depicting the 2 dimensional honeycomb lattice of graphene and how a (5,3) carbon nanotube is formed from the chiral vector [6]

the chiral vector and the unit vector $a_1$. This direction is the zigzag direction of the graphene sheet. Two different types of non-chiral nanotubes can exist. These are zigzag nanotubes and armchair tubes. They are identified by the fact that in these tubes, the honeycomb lattice of graphene always lies parallel to the tube axis. Zigzag tubes are formed when the chiral angle is equal to zero and armchair tubes form when the chiral angle is equal to thirty degrees. From theoretical studies, it has been shown that armchair tubes are always metallic and that zigzag tubes are metallic when the following constraint on the chiral vector is met:

$$\frac{(2m+n)}{3} = integer \tag{2.3}$$

All other types of tube are semiconducting [57].

### 2.2.2 Electrical Transport Properties of Carbon Nanotubes

Experimental studies have been performed on individual single walled CNTs using scanning tunnelling microscopy. It was found that the electronic properties of the nanotubes depend on the diameter of the tubes, implying the theoretically determined dependency on the $m$ and $n$ values defining the chiral vector and chiral angle [58]. However after further investigation using atomic force microscopy it was found that most metallic single walled CNTs are not in fact metallic and possess gaps in the Fermi energy, and some armchair tubes which are predicted to be truly metallic possess pseudogaps [59]. Many features can affect the conductivity of CNTs including properties such as the curvature

of the tube and physical stresses acting on the tube [60].

Not only are certain types of tubes noted to be metallic, but by using the correct contacts, such as palladium, it has been shown that electron transport in nanotube field effect transistors ,constructed using metallic nanotubes, can be ballistic [61]. This is transport where the mean free path of an electron travelling in the tube is longer than the length of the tube itself. This means the electron can traverse the entire length of the tube without scattering. Behaviour known as diffusive transport in which scattering does occur within the length of the nanotube has also been experimentally observed using electrostatic force microscopy and scanned gate microscopy [62]. Metallic behaviour is seen in both individual CNTs and in as synthesised ropes and it has been found that doping of nanotubes further enhances the already impressive conductive properties of these ropes[63]. Studies on the scattering mechanisms in metallic nanotubes using atomic force microscopy have been performed. In the low bias regime it has been found that scattering is dominated by acoustic phonons whereas in the high bias regime scattering is dominated by optical and zone boundary phonons [64]. Conventional IV characteristic measurements have confirmed these results and also demonstrated the extremely high current densities that individual metallic nanotubes are capable of carrying. These are found to be in excess of $10^9$ A/cm$^2$ [65]. Magnetotransport measurements have been performed on multiwalled CNTs and Aharonov-Bohm oscillations have been detected when the magnetic field is parallel to the tube axis [66]. Magnetoresistance measurements have also shown effects of weak localization in single walled CNTs [67].

Semiconducting tubes are of great interest as they will be the building blocks of future nanoelectronic devices. It has been found that as synthesised bundles of semiconducting CNTs can conduct via a number of different mechanisms, ranging from hopping conduction to thermally activated models [68]. However these properties can be modified via chemical doping and new behaviours have been observed such as transitions to metallic behaviour [69], [70], [71]. Hopping conduction has been observed in magnetotransport measurements, but other mechanisms, such as thermally activated transport, have can been seen in these samples. Different mechanisms are dominant in different temperature intervals [72]. Another important transport mechanism found to dominate in optically transparent samples is Coulomb gap variable range hopping. This has been observed in resistance and magnetotransport measurements [73]. Effects of charge localization have been recorded in bundles of semiconducting CNTs. The localization has been attributed to disorder within the bundles themselves [74]. Localization and scattering effects have also been studied by performing conducting channel length dependent resistance measurements [75].

These and other novel and tuneable electronic properties of CNTs mean they may provide a way to construct nanoelectronic devices such as field effect transistors, diodes and voltage inverters, with a number of reviews being written on the topic [76], [77], [78]. CNTs can be used to construct a transistor by capacitive coupling to an electrostatic backgate. Common materials used for this include silicon dioxide. By changing the voltage across the back gate either n type of p type behaviour can be observed from the transistor [79]. One feature that limits the functionality of these devices is the Schottky barrier that exists at the metal-nanotube interface. Research has been done to determine the ideal nanotube diameter and metal contact to optimize device performance by minimizing the Schottky barrier [80].

The one dimensional nature of CNTs makes them ideal candidates to study novel phenomena of quantum transport. At very low temperatures of approximately 10 K single electron transport has been observed in bundles of single walled CNTs. These measurements also displayed features of a Coulomb blockade [81]. Proximity induced superconductivity was detected in both individual and bundles of single walled CNTs contacted with superconducting electrodes. This effect was only observed in extremely low temperatures of less than 1 K [82]. Luttinger liquid behaviour has been observed in the differential conductance measurements of single walled CNTs at low temperatures. More work needs to be done to truly understand these results as both Luttinger liquid behaviour and Fermi liquid behaviour have been observed in the same samples [67]. Other interesting features such as the detection of quantum dots and the observation of Kondo physics have been observed in CNTs and these materials provide a platform to study these phenomena in much greater detail [77].

## 2.3 Electrical Transport in Carbon Microspheres

Since the overall properties of CMSs are still under investigation, their electrical transport properties are still very poorly understood. Reports of the electrical transport properties of boron doped and pristine CMSs are in the literature [7]. Resistance measurements showed that Mott variable range hopping (VRH) is the dominant conduction mechanism in pristine CMSs. The same model was applied to the resistance measurements obtained for boron doped CMSs and good correspondence was found at temperatures higher than 170 K. At lower temperatures the doped sample showed a much lower conductivity than the pristine sample. It has been suggested that this reduction in conductivity can be attributed to charge localization. Figure 2.7 shows the resistance measurements taken for the pristine and boron doped samples with the Mott VRH model fitted to the data.

Other studies were performed on carbon nanoparticles synthesised from the graphitization of nanodiamond. These samples were found to conduct via 2 dimensional Mott VRH. Resistivity measurements in conjunction with magnetotransport measurements were used to determine the mean free path of carriers in the samples. These were determined to be 10 and 100 Angstrom across the samples studied. The carrier concentration of the samples was also obtained from these measurements and was found to be of order $10^{21}$ $cm^{-3}$ [83]. CNSs have also found use in the search for higher transition temperature superconductors. Iron nanoparticles encapsulated by CNSs were used to dope magnesium diboride in an attempt to increase the critical current density and increase the transition temperature of the superconductor. While no large change was observed in the transition temperature, an improved critical current density of 1100 $kAcm^{-2}$ was obtained [84]. Conductivity measurements have been performed on individual CMSs synthesised from polyethylene and polystyrene waste. These measurements were achieved by attaching two nanoprobes from a SEM to the CMS. The conductivity of the individual sphere was measured to be 45 S/m [85]. Quasi one dimensional behaviour has been observed in chains of self-assembled conducting carbon nanoparticles. These structures also exhibited Coulomb blockade behaviour at temperatures below 77 K [86].

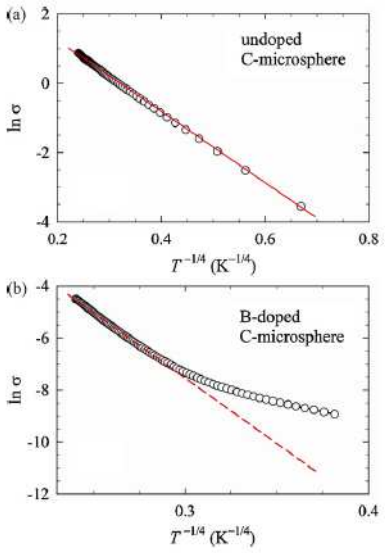


Figure 2.7: Resistance measurements of pristine and boron doped carbon microspheres showing variable range hopping fits to the data [7]

The electrical transport properties of materials such as carbon black have been studied intensely, mainly in the form of carbon black - polymer composites. These systems are usually studied in the context of percolation theory using ac measurements, but dc resistivity measurements have been performed on some samples. It has been shown that conduction in these samples is governed by mean field behaviour, but the temperature dependent resistance behaviour cannot be explained by percolation theory alone [87].

Resistance measurements performed on carbon black-epoxy resin composites have shown that both Coulomb gap VRH and fluctuation induced tunnelling (FIT) can account for the data equally well at low temperatures. This has been interpreted as hopping occurring between sites inside areas of carbon black and tunnelling occurring through regions of insulating epoxy resin [88]. Similar behaviour involving competing hopping and tunnelling mechanisms have been seen in novel conducting nanoporous carbon particles. In this case the non-ohmic IV characteristics of the samples provided further evidence of the tunnelling behaviour [89]. Coulomb gap VRH has also been observed in these kinds of systems [90] as indicated by both resistance and magnetotransport measurements. Pure tunnelling behaviour has also been observed [91] as well as conventional Mott VRH with high dimensionality brought about by super localization [92]. A transition from coulomb gap VRH to FIT has been observed in carbon onions. These readings were confirmed with results from wide frequency ac conductivity measurements [93]. Impedance spectroscopy has also been used to study the conductivity of carbon blacks as a function of compression and the conductivity was found to be directly related to the density of the carbons [94].

A primary area of application of CSs is as electrode materials in electrochemical cells. Many studies on the electrical properties of CMSs are related to this research. CoO nanoparticles encapsulated by hollow graphitic CSs have shown reversible capacity of 584 $mAhg^{-1}$ at a constant current density of 100 $mAg^{-1}$ between 0 and 3.0 V [95]. Mesocarbon microbeads have been used in similar applications and measurements were performed on a single mesocarbon microbead injected with lithium ions [96]. A novel form of hollow CS fabricated from nanographene has been used as an anode material in lithium ion cells and has shown an even greater reversible capacity of 600 $mAhg^{-1}$ [97]. It is believed that these hollow spheres perform better than solid spheres because of a higher surface area, shorter path distance for lithium ion transport and more freedom for volume change [98].

Another area of application for CNSs is in super capacitors. Studies performed on CMSs synthesised from ultra-sonic spray pyrolysis of aqueous precursors have shown higher electrochemical double-layer capacitance than other carbon structures. The highest capacitance observed was 360 $Fg^{-1}$ and the capacitance is thought to be a result of surface functionality [99]. Mesoporous CNSs with added nitrogen functional groups have been studied and compared to conventional carbon blacks, non-functionalized CNSs and polypyrrole nanospheres. The functionalized nanospheres showed a greatly improved reversible specific capacitance of 240 $Fg^{-1}$ [100].

## 2.4 Models of Electrical Transport

There are many models that exist to explain the movement of charge carriers through a medium. These range from percolation theory [101] to theories of quantum transport [102]. For the purposes of this study, transport mechanisms in the hopping regime will be discussed due to the success such models have found in explaining transport phenomena in bulk carbon nanomaterials as discussed in previous sections. Transport in the hopping regime is semi-classical in nature. Two models that will receive particular attentions are VRH and FIT.

### 2.4.1 Variable Range Hopping

Hopping conduction is a form of electrical transport where electrons traverse a material by hopping from one localized state to another. Electrons can move to states of a higher energy, equal energy or a lower energy. This type of conduction is prevalent in disordered systems. When hopping occurs to a higher energy state, energy is required and is obtained from thermal fluctuations. When hopping occurs to a lower energy state, excess energy is emitted in the form of a phonon. In order for hopping to occur, the occupied and empty states must be available, meaning that hopping may occur near to the Fermi level. However this is not a necesary condition as excitation can occur across a relatively wide band gap with neither of the edges near the Fermi level and VRH may also be the dominant conduction mechanism in systems where the Fermi level is not definable. Overlapping of the wave functions of the two localized states is also required. The model was first proposed by Mott in the context of nearest neighbour states and hopping between states of varying distances [103].

#### Nearest Neighbour Hopping

This occurs when an electron obtains energy to hop from its current localized state to the nearest localized state above its current state. The thermal energy of the electrons limits the rate of conduction. In this situation, electrons in localized states cannot obtain the energy needed to move to the conduction band. At low temperatures, the energy provided from thermal fluctuations isn't enough. However, it can arise that the energy difference between the current localized state and the nearest neighbour localized state is smaller than the activation energy between the current localized state and the conduction band. It should be noted that the thermal energy of an electron is an average over its statistical

components. One may argue that at low temperatures, the excitation rate of phonons is largely diminished which in fact aids this kind of transport. The distance between these localized states, given by $d_{nn}$, is dependent on the concentration of localized states, given by $N_{LS}$. This dependency is given by:

$$d_{nn} = \left(\frac{3}{4\pi N_{LS}}\right)^{\frac{1}{3}} \tag{2.4}$$

When hopping occurs a phonon of energy $E_{hop}$ is absorbed. The conductivity that results from nearest neighbour hopping as determined from percolation theory calculations is given by:

$$\sigma_{nn} = C_{nn} \exp\left(-\frac{\alpha d_{nn}}{a_d}\right) \exp\left(-\frac{E_{hop}}{kT}\right) \tag{2.5}$$

where $a_d$ is the spatial extent of the wave function, $\alpha$ and $C_{nn}$ are temperature independent constants, $T$ is the temperature of the system and $k$ is the Boltzmann constant. The second exponential in the above equation is related to the thermal activation energy required for hopping to occur whereas the first exponential is related to the overlap of the wave functions of the two localized states.

### Variable Range Hopping

The case described above can be applied in situations where the two localized states are both close in distance and energy, however situations may arise where localized states exist which are further away in distance from the current state but require less energy for hopping to take place. In these cases the probability for hopping to occur between the current state and the localized state a further distance away may be higher. These situations arise at very low temperatures and the average hopping distance $d_{vr}$ increases with decreasing temperature. The temperature dependency is given by:

$$d_{vr} \approx a_d \left(\frac{T_0}{T}\right)^{\frac{1}{d+1}} \tag{2.6}$$

where $d$ is the dimensionality of the system and $T_0$ is the characteristic temperature. The characteristic temperature contains information regarding the density of states at the Fermi level. The conductivity that results from VRH is determined by Mott's law

and is given by:

$$\sigma_{vr} = C_{vr} \exp\left[-\left(\frac{T_0}{T}\right)^{\frac{1}{d+1}}\right] \tag{2.7}$$

where $T$ is the temperature of the system and $C_{vr}$ is a temperature independent constant. The activation energy may be obtained from taking the following derivative:

$$E_{act} = -\frac{d(\ln \sigma)}{d(kT)^{-1}} \tag{2.8}$$

The activation energy monotonically decreases with decreasing temperature.

#### Efros-Shklovskii Variable Range Hopping

Efros *et al* [104] argued that at low enough temperatures the Coulomb interaction between localized electrons will introduce a gap in the density of states at the Fermi level. The introduction of this gap would influence Mott's law of hopping conductivity which was derived under the assumption of a constant density of states. The most significant change to Mott's law is a modification to the temperature dependency for the conductivity in such a system. The expression for conductivity in such a system is given by:

$$\sigma_{es} = C_{es} \exp\left[-\left(\frac{T_0}{T}\right)^{\frac{1}{2}}\right] \tag{2.9}$$

where $C_{es}$ is a temperature independent constant and $T_0$ is the characteristic temperature and contains information regarding the density of states at the Fermi level. This expression is similar to the Mott VRH expression for one dimensional systems, however Efros-Shklovskii variable range hopping (ES-VRH) remains unchanged irrespective of the dimensionality of the system being studied.

### 2.4.2 Fluctuation Induced Tunnelling

FIT is a model of thermally activated conduction in disordered systems originally proposed by Sheng [105]. This transport mechanism models a material as a series of al-

ternating conducting and non-conducting segments. At higher temperatures, electrons are able to move over the potential barriers of the non-conducting regions with energy provided from thermal fluctuations. At lower temperatures the electrons do not have sufficient energy to surmount the barriers and as a result they tunnel through them. The resistivity of a system that conducts via FIT is given by:

$$\rho(T) = \beta \exp\left(\frac{T_b}{T_s + T}\right) \tag{2.10}$$

where $\beta$ is a weak function of temperature that contains information regarding the barrier height that separates metallic regions and other properties of the network structure of the material. It also contains information regarding the geometry of the material. It can be taken as a constant compared to the temperature dependence of the exponential. $T_s$ is the temperature above which thermal fluctuations become a competing factor and allow for conduction over the potential barrier. $T_b$ is a much more complicated quantity which is dependent on the barrier shape and height and is affected by the local electric field and the image force. It relates to the temperature below which tunnelling through the potential barriers is the dominant conduction mechanism.

# 3 Sample Synthesis and Characterization

In this chapter the experimental details of sample synthesis and sample characterization will be discussed. A description of the sample synthesis technique will be presented and the parameters used for sample synthesis will be given. This is followed by a discussion of the characterization experiments performed on the samples that resulted from the synthesis process. The characterization experiments discussed will include SEM, Raman spectroscopy and EPR spectroscopy. Limited detail will be provided as the results of this work will be covered in more detail elsewhere.

## 3.1 Sample Synthesis

A common method for the synthesis of CMSs and carbon nanomaterials in general is via a CVD reaction [106], [107], [41]. This is because no metal catalyst is required for synthesis, reducing the need for purification once synthesis is complete [108]. This is particularly useful for the synthesis of doped samples. Yet another advantage of this technique is that large quantities of product can be produced from CVD reactions [109]. In light of these advantages, a lot of effort has gone in to determining optimal synthesis parameters, such as precursor flow rates and furnace temperature [8].

The detailed chemistry occurring in any CVD reaction is complex and the process requires fine tuning of many parameters in order to ensure the correct reaction is occurring. In simple terms a conventional CVD reaction will involve precursor gases being introduced into a reaction chamber. Here the precursors interact with a heated substrate where a solid phase will form and will be deposited on the substrate [110]. The most basic CVD reactor will consist of a gas source, a reaction chamber encased in a furnace and an exhaust [111]. The inclusions of pumping systems for low pressure CVD and high voltage sources for plasma enhanced CVD are common ways to improve the efficiency of reactors and extend their functionality.

Sample synthesis was achieved via the pyrolysis of acetylene in a horizontal chemical vapour deposition (h-CVD) reactor. Figure 3.1 shows a schematic diagram of the reactor used. The source of nitrogen dopant was acetonitrile. First the reactor was flushed with argon gas to ensure a clean environment for synthesis. The furnace was allowed to reach a temperature of 850 °C before the precursors were introduced. Argon was used as the carrier gas for the introduction of the acetylene into the reactor with a flow rate of 100 ml/min. To complete the introduction of precursors into the reactor, acetonitrile was then allowed to flow with the carrier gas. The system was then left to react for 2 hours. Other runs were performed with an elevated furnace temperature of 900 °C. Upon completion of the reaction, samples were collected from different parts of the reactor. Some samples were collected from the inside of the quartz boat positioned in the centre of the furnace, while others were collected from the lining of the quartz tube making up the inside of the reactor. In total 4 samples were collected from the reaction.

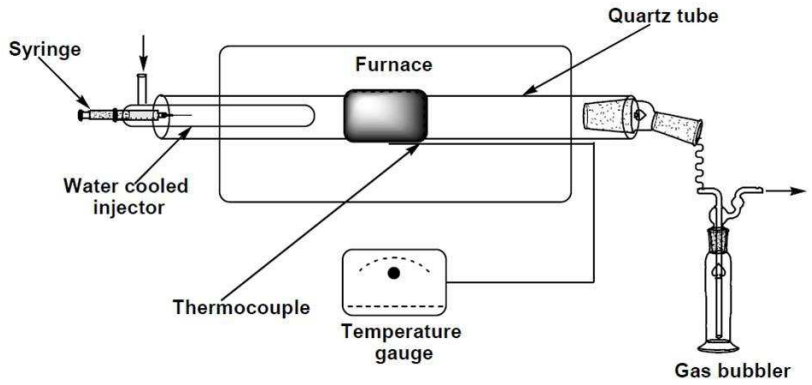


Figure 3.1: A schematic diagram of the horizontal chemical vapour deposition reactor used for sample synthesis [8]

## 3.2 Characterization

Once the reaction was completed, the resulting product is a black powder. This powder could contain any number of different carbonaceous products. Therefore a number of experiments must be performed on the samples to probe their microscopic properties. This will determine if the reaction had indeed resulted in the desired products.

### 3.2.1 Scanning Electron Microscopy

SEM is a common characterization technique as it allows for the microscopic physical structure of a sample to be observed in the form of an image [112], [113], [114]. In principle this is achieved by focusing a narrow beam of electrons emitted from the microscope onto a point on the sample. The beam is then made to move over each point on the sample being studied. This process is called scanning. Some of the electrons are reflected from the object, others are scattered or absorbed. The resulting electron current being reflected by the sample is collected. This current is then amplified and used to define the brightness of a cathode ray tube. The beam in the cathode ray tube is moving in correspondence with the beam of electrons scanning the sample. Any changes in the object which causes a change in the reflected beam of electrons will be recorded in the form of a change in brightness on the screen of the cathode ray tube. This can be due to secondary emission of electrons, but altering the angle of incidence of the electron beam allows for purely topographical information to be obtained [115].

The samples were given the designation SD1, SD3, SD4 and SD5. Electron microscope images of the samples were taken with a Topcon SM510 Scanning Electron Microscope. Figure 3.2 shows the high and low magnification images of all the samples used in this research. Large agglomerates of particles can be seen in images with a lower magnification of approximately 500×, as seen in the insets of Figure 3.2 A-D. The particles form long strands and groups as they have a tendency to chain together due to Van der Waals forces. The spherical shape of the constituent particles can clearly be seen in the higher magnification images of approximately 5000×. The distribution in measured diameters for the spheres was determined by analysing the size of particles at different sites in the sample. 3 of the samples, SD1, SD3 and SD4, all have a similar distribution of spheres diameters, the largest being approximately 2.6 $\mu$m and the smallest being 750 nm. SD5 however has a much larger distribution of sphere diameters, the largest being approximately 3.8 $\mu$m and the smallest being 750 nm. After analysing the sphere diameters in a number of sites, the average sphere diameter across the sample suite was determined to be 1.7 $\mu$m $\pm$ 0.4 $\mu$m. This analysis confirms that the reaction did in fact produce microspheres.

### 3.2.2 Raman Spectroscopy

Raman Spectroscopy is a not only a common characterization technique used when synthesising carbon nanomaterials, but it is also an important tool for probing the structural properties of these materials [116], [112], [117]. Raman scattering is a form of inelastic

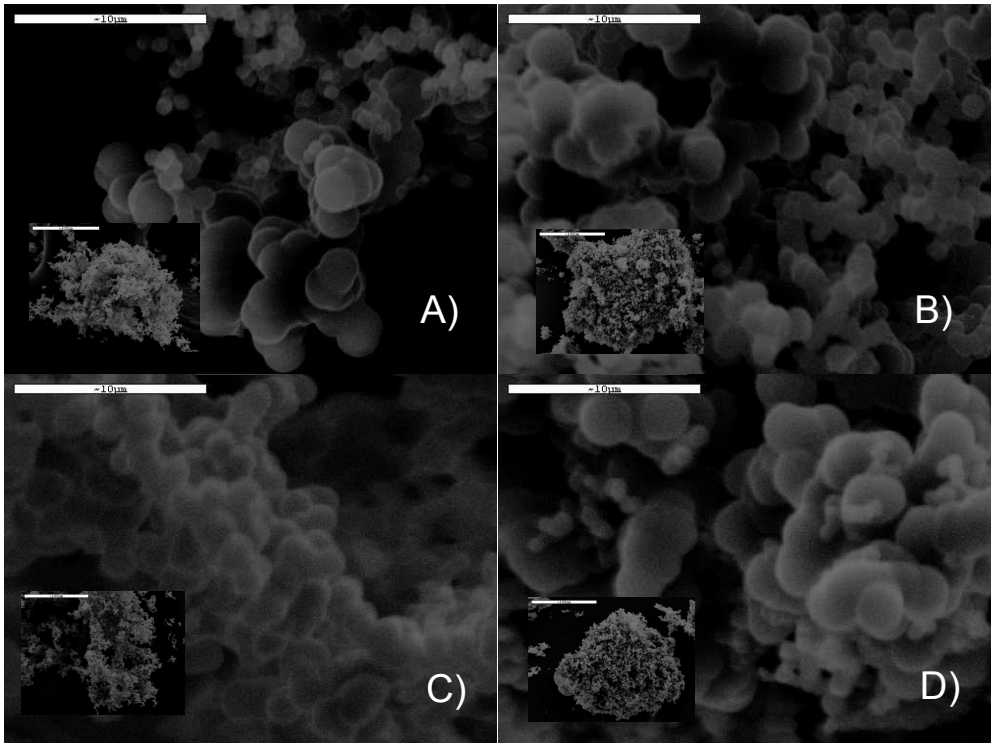


Figure 3.2: Scanning electron microscope images of the samples after synthesis at 5000× magnification. In each case, the inset is the sample at 500× magnification A) SD1 B) SD3 C) SD4 D) SD5

scattering between a sample's constituent molecules and incident monochromatic light. If the frequency of the scattered light is analysed it will be found that some of the scattered light will have a lower frequency than the incident light and some of the scattered light has a higher frequency than the incident light. This shift in frequency is due to the exciting or de-exciting of the molecules into virtual vibrational modes. Raman scattering is a very weak effect compared to elastic Rayleigh scattering and so filters must be used to remove the overpowering effect of Rayleigh scattering. The shifts in frequency observed from Raman spectroscopy can provide information regarding the molecular structure of the sample being studied as well as the chemical environment of the sample [118].

Raman spectroscopy measurements were performed on all samples using a 514 nm laser excitation light source. Common features include major peaks observed at 1381 $cm^{-1}$ and 1595 $cm^{-1}$ with a minor peak at approximately 1200 $cm^{-1}$.The two dominant spectral lines, known as the D and G bands, indicate the presence of a graphitic carbon structure in the samples [119]. The G peak represents the doubly degenerate $E_{2g}$ phonon mode which is a feature of $sp^2$ hybridized carbon. The D peak results from defects in the carbon structure [120]. The spectra obtained from these samples are comparable to those seen for CNSs [121], [112]. Figure 3.3 shows a representative spectrum of the sample SD3

at 514 nm laser excitation wavelength. Full details are provided elsewhere in another student's thesis which is yet to be completed.

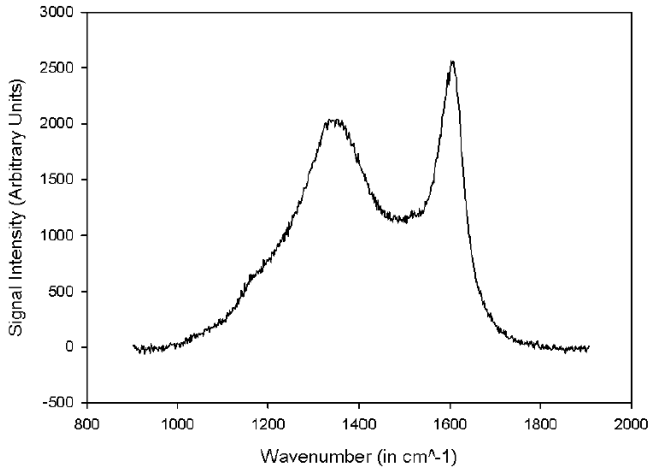


Figure 3.3: Representative Raman spectrum of the sample SD3 at 514 nm laser excitation wavelength

### 3.2.3 Electron Paramagnetic Resonance Spectroscopy

Like Raman Spectroscopy, EPR Spectroscopy is not only used as a characterization technique when synthesising different nanomaterials, but it is also used to probe the magnetic properties of these samples [117], [122], [123]. EPR spectroscopy exploits the principles of magnetic resonance to obtain a spectrum of the sample being studied. The sample is placed inside an external magnetic field of an appropriate magnitude to induce Zeeman splitting of the degenerate spin states of unpaired electrons in the sample. The sample is then bombarded with microwave radiation of an appropriate energy which matches the energy gap between the split spin states. This induces a transition from the lower energy state to the higher energy state. This net absorption of energy by the sample is what is detected and produces the spectrum obtained. Since the spin of the unpaired electrons is related to their magnetic moments, the spectrum provides information about the magnetic properties of the sample. Because unpaired electrons are the focus of study in EPR experiments, some information regarding the conductive properties of the sample can be obtained. If pulsed experiments are performed, the spin dynamics of the sample can also be probed [124].

The EPR spectrum for the n-CMSs was acquired using a Bruker ESP 300E spectrometer in continuous wave mode. The resonance signal is slightly Dysonian indicating the presence of conduction electrons [125]. The spectrum obtained is comparable to those for

| Sample | Nitrogen Concentration |
|---|---|
| SD1 | $(1.7 \pm 0.5)\%$ |
| SD3 | $(3.4 \pm 1)\%$ |
| SD4 | $(3.4 \pm 1)\%$ |
| SD5 | $(1.7 \pm 0.5)\%$ |

Table 3.1: Nitrogen concentration of the samples as obtained from electron paramagnetic resonance spectroscopy measurements

doped CNTs [126], [127] and pristine CNSs [41], [85]. Figure 3.4 shows a representative spectrum of the sample SD3.

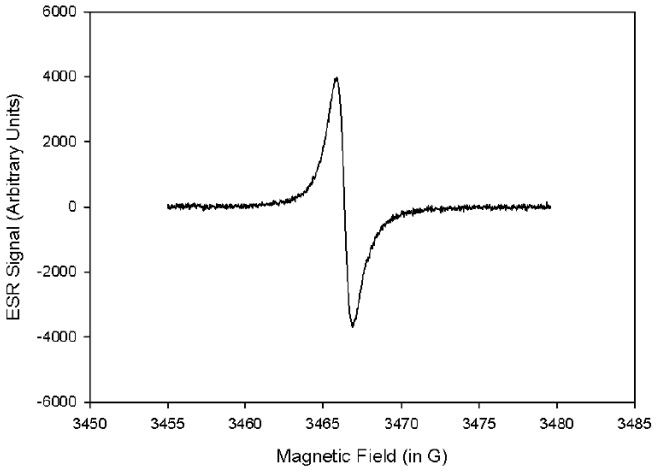


Figure 3.4: Representative electron paramagnetic resonance spectrum of the sample SD3

A novel technique was developed to determine the nitrogen concentration of the samples using the EPR spectrometer [128]. Spectra of a set of CSs produced with similar conditions but with different nitrogen concentrations were collected. The nitrogen concentrations of these samples were determined using CHN analysis. The amplitude of each sample's spectrum is divided by the mass of the sample being analysed. This provides the spin concentration per unit mass of the sample and can be used as an indicator of the amount of substitutional nitrogen in the sample. These results provide a rudimentary calibration curve for the spectrometer which allows for the nitrogen concentrations of unknown samples to be determined. Figure 3.5 shows the calibration curve obtained for the spectrometer. Table 3.1 shows the nitrogen concentrations of the samples once the calibration curve was applied to them. The errors are large due to the small size of the sample used and the difficulties associated with spin-concentration EPR experiments. The complete set of results from the EPR experiments performed on the samples, apart from characterization, are beyond the scope of this work.

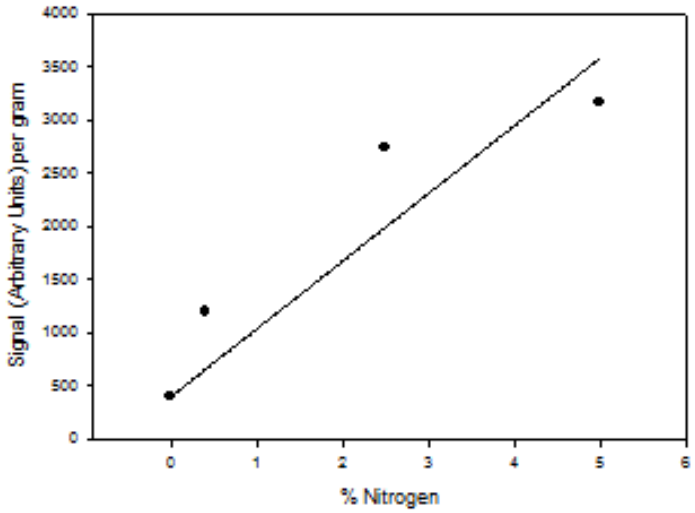


Figure 3.5: Calibration curve for the concentration of paramagnetic nitrogen in nitrogen doped carbon microspheres

# 4 Experimental Apparatus

In this chapter, the general details of the experimental process followed for data collection will be elaborated on. First a description of the common pieces of apparatus will be given, followed by a discussion of the specific requirements of each experiment conducted, namely the IV characteristics of the samples, resistance measurements and magnetoresistance measurements. This will be followed by a section which will explain the sample preparation procedure which was essentially unaltered between experiments. Subtle differences between experiments will be highlighted where necessary. The process of taking readings for each experiment will then be explained. Finally a section detailing the methods used for processing the data will be given.

## 4.1 Common Experimental Apparatus

While the experiments conducted for this dissertation had certain features in common, subtle differences between the requirements of each type of measurement necessitates a discussion of the common apparatus used throughout the experimental process as well as the specific equipment used in each experiment. The common pieces of apparatus used for conducting experiments include the sample probe, sample holder, cryogenic system and the intelligent multiplexer. With the exception of the cryogenic system all of these were designed and built in house in the laboratory and by the physics department workshops.

### 4.1.1 The Sample Probe

Figure 4.1 shows a schematic drawing of the probe used to perform the IV characteristics, resistance measurements and magnetoresistance measurements. A description of the various components it consists of follows:

The probe head consisted of a brass plug, which had 2 sets of male Oxford 10 pin connectors attached to the top to allow for all relevant electrical connections to be made. The

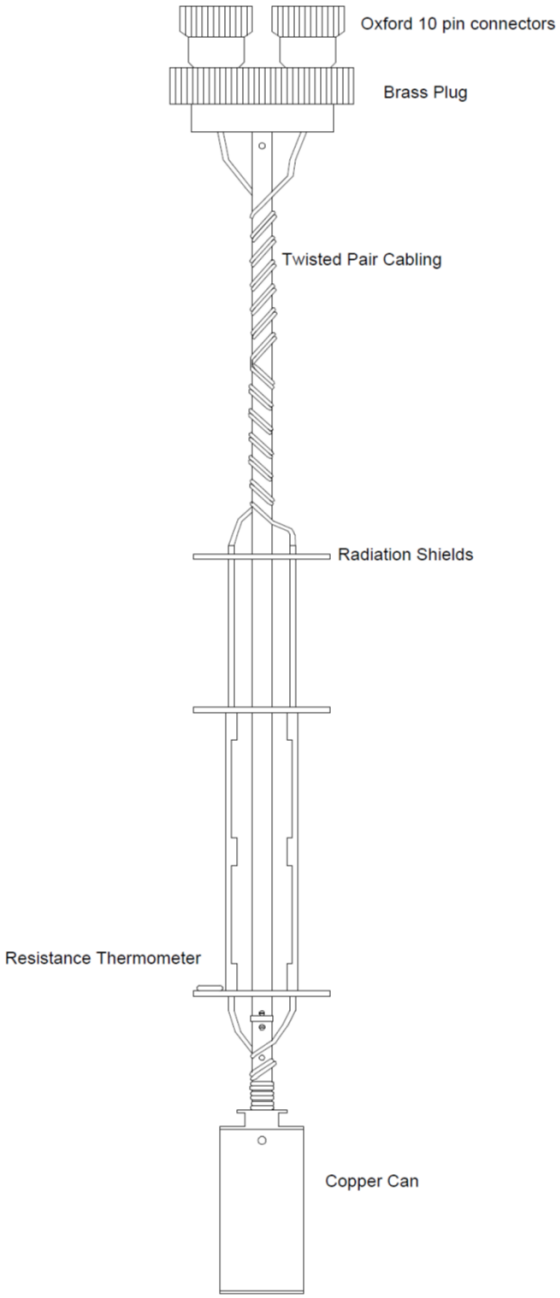


Figure 4.1: A schematic diagram of the cryogenic probe used to take low temperature transport measurements. Adapted from [9]

points of contact between the connectors and the brass plug were sealed with an epoxy resin to ensure that no cryogens could leak from the cryostat. The brass plug also acted as a seal, preventing cryogens from leaking from the cryostat. A thin walled stainless steel tube was connected to the underside of the brass plug. This tube would extend down into the base of the cryostat. There were holes drilled into the tube to allow for gas exchange and there were 3 stainless steel spacers which allowed the probe to remain stable in the cryostat under cryogen flow and also acted as radiation shields. There were holes drilled in the spacers to further allow for gas flow.

Electrical connections were fed down to the bottom of the probe by using electrical leads shielded by a plastic coating. Each coating contained 10 insulated copper wires that were wound in a twisted pair arrangement in order to reduce electrical interference. The protective coating was wound around the stainless steel tubing in order to increase the length of the wires and reduce the heat loading at the base of the probe.

At the first spacer, the plastic tubes separated and each entered a separate metal tube. The metal tubes acted as guides for the copper wires and there were sections of the tubes missing which exposed the insulated copper wires to the cryogen flow which cooled them and reduced the heat load at the base of the probe.

On the tapered end of the stainless steel rod inside the copper can, there was a LakeShore Carbon Glass resistance thermometer which allowed for the temperature at the base of the probe to be measured. This allowed for a more accurate measure of the sample temperature to be obtained. On the spacer nearest the base of the cryostat there was another LakeShore Carbon Glass resistance thermometer. This thermometer was used in experiments with liquid helium to determine when the copper sample chamber had been submerged in liquid helium. This thermometer was not used in this research.

At the base of the probe a copper sample chamber was connected that could be removed to allow for positioning of the sample. Copper was chosen as a material as it has a high thermal conductivity and allows for a constant temperature environment for the sample to be created. The sample chamber also protected the sample from the convection currents in the cryogen flow. There were a number of holes drilled in the base of the copper sample chamber to allow for gas exchange. This ensured efficient cooling of the sample and prevented the occurrence of $CO_2$ and $H_2O$ solidification. The central hole allowed for the mounting of the powdered sample cell. This further ensured that the sample would be disturbed as little as possible by movements during transport of the probe to the cryostat and during experiments by currents in the cryogen flow. Nitrogen uptake was not considered in these experiments, but will be considered when performing future measurements.

Electrical contact was made to the sample by 4 wires that were connected to the wires leading to the top of the probe via 4 tabs protruding from the underside of the top of the copper sample chamber. Each voltage sense wire was soldered to a current carrying wire and the resulting wire arrangements were wrapped in Teflon tape to provide electrical insulation. These wires would then be mechanically anchored to the Teflon sample holder.

### 4.1.2 The Teflon Sample Holder

Figure 4.2 shows a schematic drawing of the Teflon sample holder used to perform the IV characteristics, resistance measurements and magnetoresistance measurements. A description of the various components it consists of follows:

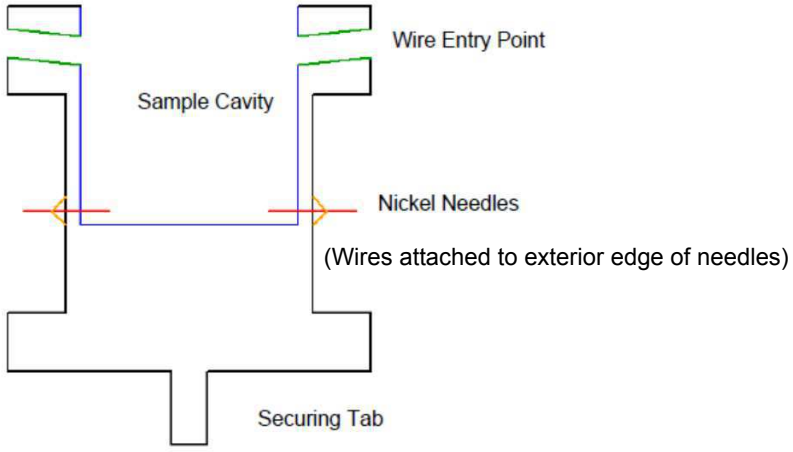


Figure 4.2: A schematic diagram of the Teflon sample holding cell used to contain the powdered sample being studied

A cylindrical Teflon cell was designed to contain the powdered microspheres in such a way that they could be compacted easily and the cell could be placed inside the copper can sample holder without breaking electrical contact. A cylindrical geometry was chosen to allow for ease of manufacture. If the cell were to be used to perform resistivity measurements, the van der Pawu technique could be utilized and if proper care is taken in terms of sample preparation, the cylindrical geometry should not prove to be problematic [129]. Teflon was chosen due to its insulating properties and high mechanical stability at low temperatures. Electrical contact was achieved via pressure contacts using two nickel sewing needles driven through the sides of the Teflon cell into the powder. The effect of using nickel as the contact material was only considered after measurements were performed and will be taken into account in future experiments. These nickel contacts

were secured in place using glue and the externally protruding edges were then soldered to the current carrying wires of the probe. The nickel contacts were used as previously the free hanging copper wires were used to make direct electrical contact with the sample and keeping the wires secure in the sample proved to be very difficult. Conventional glue was used to secure the nickel contacts as it is inexpensive and stable at low temperatures. The glue was necessary to prevent movement of the contacts in the sample and to ensure that no powder could escape through the holes made by the nickel contacts in the Teflon. However special care had to be taken to make sure that the glue did not get wet as if it did it would lose its adhesive properties. A securing tab protrudes from the base of the cell. This tab would be inserted in a hole in the base of the copper can. This ensures that the cell remains stable inside the copper can and the sample will not be disturbed should any movement occur.

### 4.1.3 Intelligent Multiplexer

Figure 4.3 shows a component diagram of the intelligent multiplexer designed and built to perform the IV characteristics, resistance measurements and magnetoresistance measurements. Figure 4.4 shows a flow diagram providing a simplistic explaination of how the different parts of the intelligent multiplexer interact with one another. A description of the various components it consists of follows:

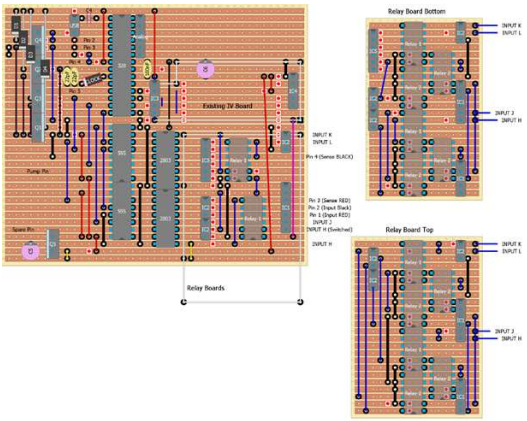


Figure 4.3: A component diagram of the intelligent multiplexer used to switch between different wire configurations for different experiments and act as a digital power supply

An 'intelligent' multiplexer was created to allow for easy automation of the experiments. It utilizes an Arduino Uno development board and an ATMEL ATmega328 microprocessor loaded with the Arduino open source bootloader to accurately control the output

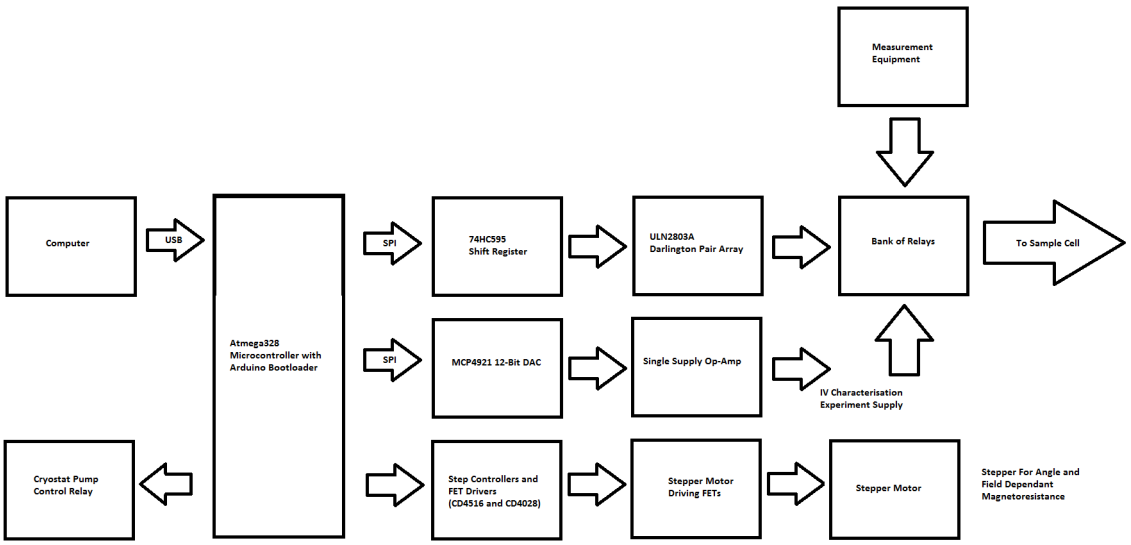


Figure 4.4: A flow diagram of the intelligent multiplexer showing how the different parts of the multiplexer interact with one another.

Voltage of an analogue 30V DC power supply. Human interaction was therefore not necessary when obtaining IV characteristics of the samples. This was achieved by connecting a set digital output pin of the Arduino to an SPI interfaced 12 bit digital to analogue converter (DAC) followed by a single supply OP amp set to a gain of 6. Using this circuit, steps of 7 mV across the sample could be achieved. A set of relays controlled by the intelligent multiplexer ensured that the different voltage line pin configurations required for each experiment (resistance, IV characteristics and magnetoresistance) could be obtained without having to physically remove wires. The intelligent multiplexer was connected to the respective measurement devices used throughout all experiments and to the multiplexer carrying signals to and from the sample. This allowed the intelligent multiplexer to make sure the correct measurement device was connected to the sample in the correct way to perform a specific kind of measurement. The intelligent multiplexer interfaced with a computer running Windows XP and was controlled using LabView code that was written to control all the apparatus and automate the experiment and data collection. The LabView program would instruct the computer to send commands to the intelligent multiplexer via a serial connection that would increase or decrease the applied voltage or select the correct wire configuration for a specific experiment. The ability to further automate the experiment was added in the form of a pump control circuit that could be controlled by the intelligent multiplexer. This circuit simply consisted of a relay that would disconnect the pump from the mains power supply when the intelligent multiplexer was given the correct command. This allowed experiments to run through the night without being physically monitored and shut off. Please see the Appendices for the code written for the ATMEL ATmega328 microprocessor written in Processing using

the Arduino development environment as well as the LabView code used to automate the experiments.

### 4.1.4 Cryogenic System

In order to perform low temperature measurements a cryogenic system was used. The components of this system were manufactured by Oxford Instruments and consist of a continuous flow cryostat, a VC31 gas flow controller, an ITC503 temperature controller, a GFS 650 transfer tube, a GF3 vacuum pump and a cryogen storage dewar that was used to store the liquid nitrogen or liquid helium used as cryogens.

The cryogen system was set up as follows: the cryogen transfer tube was carefully and slowly lowered into the storage dewar to prevent violent venting of gas due to the boiling of cryogens. The other end of the tube was then inserted into the continuous flow cryostat and screwed securely into place. A plastic gas carrier tube was used to connect the gas flow controller and the transfer tube. The gas flow controller is connected to the vacuum pump. The pump causes a pressure difference in the system which in turn causes cryogens to be pulled through the needle valve at the base of the transfer tube. The cryogens then circulate through the cryostat and cool the sample. The exhaust gas is sucked back out through the transfer tube and out through the gas control valve. This exhaust gas is then vented into the air. The outer sleeve of the transfer tube is evacuated so as to ensure efficient cryogen transfer. The rate of cryogen flow was controlled by balancing the needle valve at the base of the transfer tube and the valve on the gas flow controller. Ordinarily the needle valve would be opened a set amount (3 turns) to ensure good cryogen flow and the rate was controlled using the gas flow controller. The temperature of the cryostat interior was controlled using the temperature controller. The temperature controller monitored the cryostat temperature using a thermocouple. An Oxford film heater is wrapped around the vapourizer at the base of the cryostat, the electrical leads of which are connected to the temperature controller. Using this heater, the temperature controller could control the temperature of the cryogens entering the cryostat and therefore change its internal temperature. The temperature of the carbon glass resistance thermometer near the sample was measured using a LakeShore 234D Temperature Monitor. The temperature controller thermocouple was placed near the heater at the base of the cryostat whereas the temperature monitor thermometer was placed closer to the sample and provided a more accurate sample temperature.

## 4.2 Specific Experimental Apparatus

Each experiment required sets of apparatus that were similar, but needed to be connected in a different way. Figure 4.5 shows a schematic diagram of the general experimental set up used. A discussion of the apparatus required for each experiment, the purpose of each piece of apparatus and how the different components were connected for each experiment is also given.

### 4.2.1 IV Characteristics

Figure 4.6 shows a simple circuit diagram depicting how the IV characteristics of a sample were measured. A power supply is used to create a voltage drop across the sample to be studied. A voltmeter connected in parallel to the sample is used to measure what the voltage drop across it is. Since the only component in the circuit of significant resistance is the sample, only one voltmeter is necessary. An ammeter is connected in series with the sample to measure the current flowing through the sample. For the same reason listed above, only one ammeter is necessary. The voltage drop across the sample is increased in consistent steps and for each step the voltage and current are measured.

The ammeters used in these experiments were an HP34401A digital multimeter and an HP3457A digital multimeter. The voltmeter used in these experiments was a Fluke 8840A digital multimeter. The power source used in these experiments was the intelligent multiplexer designed in the laboratory. All measurements were taken using LabView software written to automate the experiment.

### 4.2.2 Resistance Measurements

The circuit diagram for resistance measurements is identical to the one for IV characteristics. A power supply is used to create a voltage drop across the sample to be studied. A voltmeter connected in parallel to the sample is used to measure what the voltage drop across it is. Since the only component in the circuit of significant resistance is the sample, only one voltmeter is necessary. An ammeter is connected in series with the sample to measure the current flowing through the sample. For the same reason listed above, only one ammeter is necessary. Both the voltage drop across the sample and the current flowing through the sample is measured and this information used to calculate the resistance of the sample. This is the only measurement made and once it is complete, the tempera-

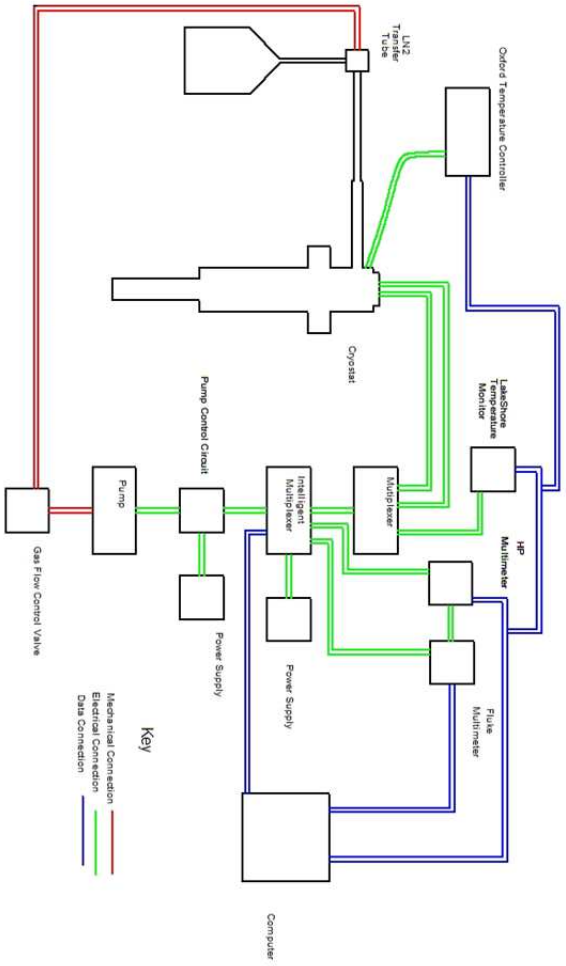


Figure 4.5: A schematic diagram of the experimental setup used to perform electrical transport measurements

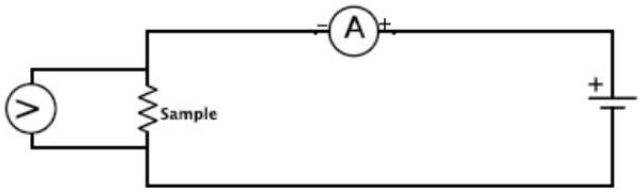


Figure 4.6: A circuit diagram of the components used to perform IV characteristics measurements

ture of the sample is changed and the same measurement taken again. The voltage drop across the sample is kept constant between changes in temperature to ensure consistency in measurements and is kept small so as to limit heating effects in the sample which will in turn alter the resistance. Current reversal was not performed in these experiments, but will be in the future.

The 4 probe resistance measurement feature of a digital multimeter was used to perform the measurements for these experiments. Two digital multimeters were used in these experiments, a Fluke 8840A digital multimeter and an HP3457A digital multimeter. All measurements were taken using LabView software written to automate the experiment.

### High Temperature Probe

Once the results of the initial resistance experiments were obtained, it was decided that it would be of interest to take readings at temperatures above room temperature. A rudimentary furnace was built in the laboratory to perform limited high temperature measurements.

The furnace consisted of an insulating outer sheath made of alternating layers of polyester material and tin foil with the reflective surface of the foil facing inwards. An Oxford film heater was secured to the outside of the copper can at the base of the cryogenic probe using Kapton tape and the sheath was placed over the outside of the copper can. The sample temperature was controlled by the ITC503 temperature controller which supplied a voltage of up to 21 V to the film heater. The temperature was measured by the temperature controller using a copper - constantan thermocouple which was placed inside the copper can and liquid nitrogen being used as the reference junction. Using this furnace, stable temperatures of up to 400 K could be reached.

### 4.2.3 Magnetoresistance Measurements

Magnetoresistance measurements are essentially the same as resistance measurements, but now the resistance measurements are performed with the sample in the presence of a magnetic field. The Fluke 8840A digital multimeter was used to take 4 probe resistance measurements as previously explained. A Varian nuclear magnetic resonance magnet was used to provide magnetic fields of up to 1.2 T for these experiments. The magnet and its power supply is an aging system which, in spite of some upgrades, provides very limited automation capabilities. A novel system to automate the magnet needed to be developed. This system consisted of an Arduino Uno development board, a Darlington array, a 15 V desktop power supply and a stepper motor. A rudimentary gearing system was developed to link the knob which controlled voltage of the magnet power supply and the stepper motor. When in constant current mode, only the voltage knob was used to control the magnetic field. The gear attached to the stepper motor consisted of a plastic bottle top sandwiched between 2 sheets of plastic. The gear attached to the voltage knob only consisted of a sheet of plastic. These two gears were connected to one another using a conventional rubber band. This meant that when the stepper motor was tuned the voltage control knob turned as well. Since the stepper motor was controlled using the Arduino Uno development board, this meant the magnet could now be controlled using a computer and the experiment could be automated.

The laboratory did not possess a gaussmeter that could be interfaced with a computer so measuring the exact magnetic field during an experiment was not possible. To overcome this problem a calibration curve was made which allowed the magnetic field to be related to the number of turns the stepper motor had made. The number of turns was translated into the number of 'steps' the Arduino Uno development board was instructed to perform which could be measured during the experiment. The magnet was calibrated across its entire range using a rudimentary gaussmeter without computer interface abilities and the calibration process was performed a number of times at different magnet temperatures so that averages of the magnetic field could be obtained and errors extracted. Figure 4.7 shows the calibration curve for the magnet. Many variables could exist in this system, for example the potential for slip in the rubber band gearing, and for more accurate results a more elegant system needs to be developed.

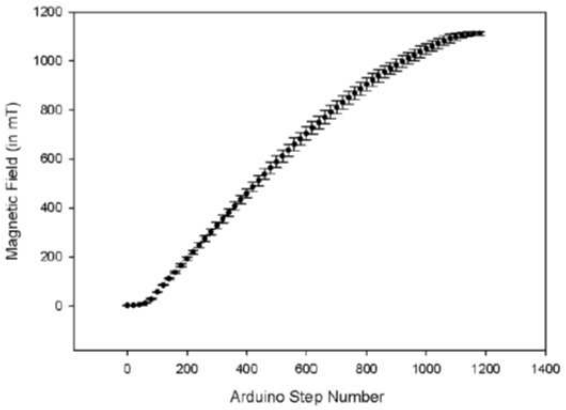


Figure 4.7: The calibration curve for the magnet used to perform magnetoresistance measurements

## 4.3 Sample Preparation

Before any experiment could be performed, the sample to be studied had to be prepared and packed into the apparatus so that the best results could be obtained. For this to occur all the components in contact with the previous sample studied needed to be cleaned so that there was no interference between results of different samples and cross contamination of the samples did not occur. This preparation process for each of the experiments performed is detailed below.

### 4.3.1 IV Characteristics

The cryogenic probe was removed from the cryostat and placed in a retort stand so that the copper can could be removed. Once the can was removed and the cell exposed a soldering iron was used to remove the solder from the copper wires and the nickel needles so the sample could be removed from the circuit. With the cell removed from the cryogenic probe the sample could now be changed. A clean needle was used to break up the compacted powder in the cell so it could be replaced in its storage container. Once the bulk of the powder was removed from the cell, the needle was used to gently scrape any agglomerated powder from the sides and crevices of the cell to ensure maximum sample recovery. The cell was then thoroughly washed with distilled water to clean out any residual sample that could not be recovered. Finally the cell was heat dried to ensure no water remained in the cell that could contaminate the sample and freeze at low temperatures.

Once the cell was thoroughly dried a new sample was packed in it. First the cell was be prepared to be inserted back into the cryogenic probe. A small needle threaded with thin copper wire was fed through the hole in the securing tab on the base of the cell. Once fed through, the ends of the copper wire were tied together. When the new sample had been prepared, the needle and copper wire was used to thread the securing tab back into the hole in the base of the copper can.

New powdered sample was introduced using a small funnel. Once a sufficient amount of sample had been added into the cell, the sample was compacted using a hand press. This was to ensure good electrical contact with the nickel needles via pressure contacts. A multimeter was then used to measure the resistance across the sample. With these bulk samples it was found that if the samples displayed room temperature resistances less than 10 k$\Omega$, there was good electrical contact between the sample and the needles and consistant results could be obtained. If the resistance was higher than this value, the sample was compressed more with the hand press and if this made no change, more sample was added and compressed further. Once an acceptible resistance was obtained, the cell can be soldered to the copper wires in the cryogenic probe and the copper can, can be replaced. Throughout this process, the resistance across the sample is constantly checked via the electrical pins at the top of the probe to ensure that electrical contact had not been broken. When the copper can had been replaced, the cryogenic probe could be placed back in the cryostat and all necessary electrical connections made. Resistance was used as the primary measure to ensure uniform packing, in future experiments, samples will be packed using the same pressure and the same amount of material is used to ensure unform packing.

### 4.3.2 Resistance Measurements

The sample preparation procedure required to perform resistance measurements is identical to that required for IV characteristics measurements.

### 4.3.3 Magnetoresistance Measurements

The sample preparation procedure required to perform magnetoresistance measurements was almost identical to that required for IV characteristics with a few subtle differences. An important parameter when performing magnetoresistance measurements was the angle between the external applied magnetic field and the direction of current flow. So it was necessary to know the direction of current flow. To accommodate for this, a small

dot was placed on the lip of the sample holding cell which was in line with the direction of current flow (in line with the nickel needles). Parallel dots were placed on each of the radiation shields and finally on the brass plug on the top of the probe. Whenever a sample was changed, all of these dots were lined up before the copper can was put back on the cryogenic probe. This was so that the direction of current flow could be known at all times outside of the cryostat and the probe could be orientated in the external magnetic field appropriately. This system is not foolproof and a new probe is being designed to facilitate the angular dependence of magnetoresistance.

## 4.4 Experimental Procedure

Each of the experiments performed had a distinct experimental procedure required which will now be discussed.

### 4.4.1 IV Characteristics

Once the cryogenic probe was inserted into the cryostat and all necessary electrical connections made, all of the required measurement devices were activated and configured to run the experiment. The intelligent multiplexer was set so the wire configuration was that required for an IV characteristics experiment and the cryogenic system was prepared. Finally the relevant LabView program was loaded and run to initiate the experiment.

Measurements were taken over the temperature range 100 K to 300 K with measurements taken every 40 K. This temperature range was chosen due to the limitations of using liquid nitrogen as a cryogen. Readings were taken every 40 K to make the code to automate the experiment simpler while still capturing the behaviour of the samples across the whole temperature range. Once the temperature was set, the system was given an hour to reach thermal equilibrium. When thermal equilibrium was reached, the voltage was increased in steps of 0.5 V. The system would wait for a brief period to allow the current reading to stabilize and then data points would be taken. Ten data points would be taken at a specific voltage with 30 second gaps between readings. This was to capture fluctuations in the data so the averages and errors could be calculated to obtain an accurate data point. Once the readings were completed, the voltage was increased and the above process repeated. Data points were collected in the range of 0 V to 24 V. Once the entire voltage range was completed, the power supply was set back to 0 V and the set temperature changed so the system could cool to the next measurement temperature.

Once the final temperature run was completed at 100 K, the pump enabling the cryogen flow was deactivated and the set temperature set to 300 K. This was to warm up the system for the sample to be changed.

### 4.4.2 Resistance Measurements

Once the cryogenic probe was inserted into the cryostat and all necessary electrical connections made, all of the required measurement devices were activated and configured to run the experiment. The intelligent multiplexer was set so the wire configuration was that required for a resistance experiment and the cryogenic system was prepared. Finally the relevant LabView program was loaded and run to initiate the experiment.

Measurements were taken over the temperature range of 80 K to 300 K for all samples. One sample had measurements taken over the range of 10 K to 300 K and another had readings taken over the range of 80 K to 340 K. Data points were taken every 10 K. Once the temperature was set, the system was given an hour to reach thermal equilibrium. When thermal equilibrium was reached 10 resistance readings were taken at time intervals of 30 seconds each. This was to capture fluctuations in the data so the averages and errors could be calculated to obtain an accurate data point. Once the data points were captured, the set temperature was changed so the system could cool to the next data point. Once the final temperature run was completed, the pump controlling the cryogen flow was deactivated and the set temperature set to 300 K. This was to warm up the system for the sample to be changed.

### 4.4.3 Magnetoresistance Measurements

Once the cryogenic probe was inserted into the cryostat and all necessary electrical connections made, all of the required measurement devices were activated and configured to run the experiment. The intelligent multiplexer was set so the wire configuration was that required for a resistance experiment and the cryogenic system was prepared. Finally the relevant LabView program was loaded and run to initiate the experiment.

Measurements were taken over the temperature range 100 K to 300 K with data points taken every 40 K. Once the temperature was set, the system was given an hour to reach thermal equilibrium. When thermal equilibrium was reached, the magnetic field was increased by turning the stepper motor a constant known amount. The system would wait for a brief period to allow the resistance reading to stabilize and then measurements

would be taken. Ten data points were collected at a specific magnetic field with 30 second gaps between readings. This was to capture fluctuations in the data so the averages and errors could be calculated to obtain an accurate data point. Once the data was captured, the magnetic field was increased and the above process repeated. Readings were taken in the range of 0 mT to 1120 mT. Once the entire magnetic field range was completed, the magnetic field was set back to 0 mT and the set temperature changed so the system could cool to the next data point. Once the final temperature run was completed at 100 K, the pump controlling the cryogen flow was deactivated and the set temperature set to 300 K. This was to warm up the system for the sample to be changed.

### 4.4.4 Data Processing

Once the data had been collected from a successful run, it had to be processed and analysed. A bulk data processing program was written in Delphi to allow for large amounts of resistance and IV characteristic data to be processed in a short space of time and eliminate the time consuming task of processing it manually.

Files created by the LabView program controlling the experiment would output data in a specific format. The data would be saved in a text file where it was arranged in columns separated by tabs. Each column contains data of a specific type, for example column 1 contains the temperature of the sample and column 2 contains the voltage drop across the sample whereas column 3 contains the current flowing through the sample. These files would be loaded into the data processing program and each line of text would then be fed into an array. String handling would then be performed on each line of text so that the relevant information could be extracted and grouped together for further processing. The arrays containing the raw data would then be processed by having averages and standard deviations calculated from the raw data of each data points and these quantities saved to a new array. Finally the processed data points were written to a new file which could be loaded into a graphing package, such as SigmaPlot, plotted and analysed. The Delphi code used to perform the data analysis can be found in the Appendices.

# 5 Results and Discussion

In this chapter the results of the experiments conducted for this dissertation will be presented. The features of these results will be discussed and important trends and anomalies will be brought to the reader's attention. Models which potentially relate the trends in the data to physical phenomena will be fitted to the data and parameters from the fits will be extracted and compared to values found in the literature. Models not originally suggested in the literature review will be explained. Deviations from the expected behaviour will be accounted for and other experiments to further the understanding of the transport properties of the samples will be suggested.

## 5.1 Resistance Measurements

Figure 5.1 shows the raw resistance measurements of all of the samples at an excitation current of 100 $\mu$A. The resistance values have been normalized to the resistance at 300 K for each sample. This is to allow for ease of comparison across the sample suite. The samples can be placed into two categories from the behaviours observed in the resistance data. The samples SD1 and SD3 can be grouped together as in these samples, pure semiconducting behaviour is observed across the entire temperature range in each case. This can be ascertained from the strictly increasing resistance with decreasing temperature [130]. The samples SD4 and SD5 can be grouped together as a transition from metallic to semiconducting behaviour is observed in their resistance measurements. Here metallic behaviour is defined as being the strictly increasing resistance with increasing temperature [130]. The transition temperature, $T_*$, is the temperature at which the change in behaviour is observed to occur. At temperatures higher than the transition temperature metallic behaviour is observed and at temperatures lower than the transition temperature, semiconducting behaviour is observed. This transition temperature has been found to vary depending on the sample under study, from lower temperatures (approximately 200 K in conducting polymer nanowires) [131] to much higher temperatures (approximately 400 K in nitrogen doped CNTs) [132]. For SD4, $T_* \approx 260$ K and for SD5, $T_* \approx 220$ K.

This transition from metallic to semiconducting behaviour forms a 'U-shape' in the measurements that has been widely reported on in the literature. Similar transitions have been observed in doped CNTs and conducting polymer nanowires [133], [132], [134]. The transition from semiconducting to metallic behaviour can be ascribed to the thermal desorption of nitrogen dopant [132]. Barnes *et al* studied the temperature dependent resistance of a number of nitrogen doped thin film single walled CNT mats. Their experiments showed the transition to metallic behaviour was not dependent on the concentration of metallic single walled CNTs in the samples. The result of altering the concentration of metallic CNTs was a shifted transition temperature, but the transition was still present. Temperature programmed desorption measurements were used to supplement the resistance data and the most likely cause of the transition to metallic behaviour was found to be nitrogen dopant desorption. Barnes *et al* found that once the samples were exposed to high temperatures for a period of time, the transition disappeared and purely semiconducting behaviour was observed. Experiments such as these could be used to further test the nitrogen dopant desorption hypothesis.

It is believed that the reason why some samples in the suite possess this transition and others do not is the variability of synthesis parameters and sample collection location. If a sample was collected from a part of the reactor where the temperature was not completely stable, this may result in the nitrogen not being bonded as strongly as it would otherwise be.

## 5.2 IV Characteristic Measurements

Figure 5.2 shows the raw IV characteristic measurements of all of the samples in the suite. The readings taken for SD5 were only taken up to voltages of 9 V as higher voltages resulted in currents that were too large to be measured by the present experimental set up. Just as was the case for the resistance measurements, the samples can be put into groups determined by the trends seen in the IV characteristics. SD1 and SD3 can be grouped together as a clear trend can be seen in the linearity of their IV characteristics with decreasing temperature. The curves start out having a strong linear component at higher temperatures and become gradually more nonlinear as the temperature decreases. An anomaly is present in the data at 300 K. This data point has a strong nonlinear component when compared to the other high temperatures observed and when compared to the lower temperature IV characteristics, the nonlinear behaviour is different.

Similarly SD4 and SD5 can be grouped together according to the trends seen in the lin-

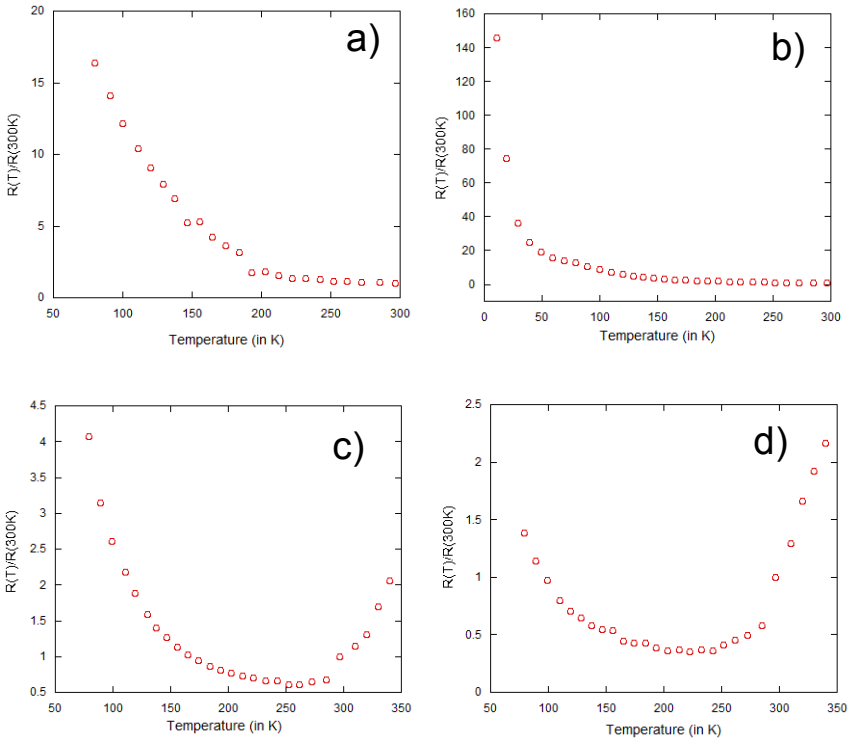


Figure 5.1: Raw resistance measurements of the samples a) SD1 b) SD3 c) SD4 and d) SD5. All resistance values have been normalized to the resistance at 300 K for each sample.

earity of their IV curves with changing temperature. At lower temperatures the same slow increase in the nonlinearity of the IV characteristics as the temperature decreases, as seen in SD1 and SD3, is observed. At higher temperatures saturation behaviour becomes evident as the bias is increased. The temperature range over which this saturation behaviour occurs corresponds to the temperature range at which metallic behaviour is observed in the samples. A similar anomaly to the ones seen in SD1 and SD3 is seen in the data at 300 K.

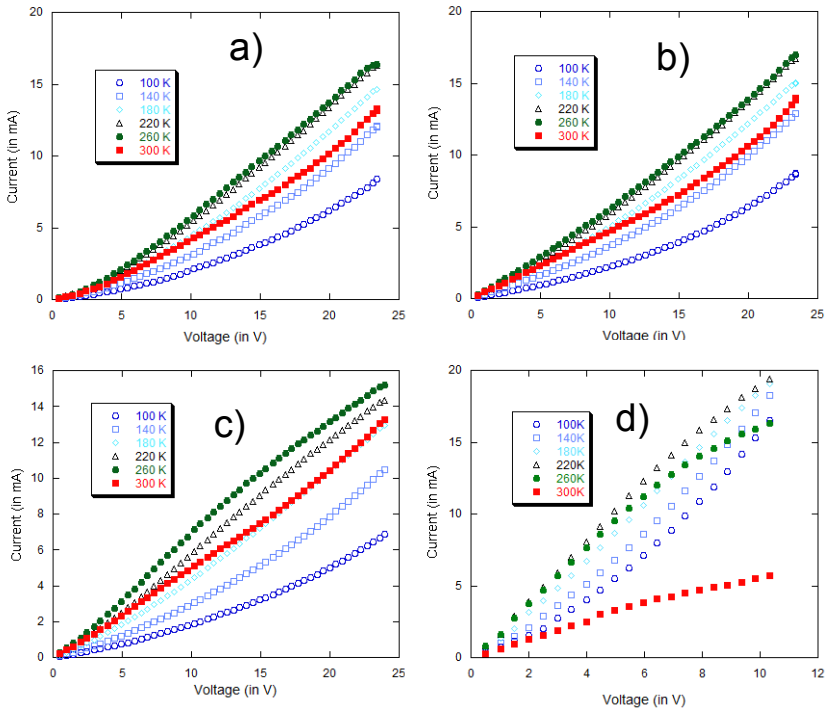


Figure 5.2: Raw IV characteristic measurements of the samples a) SD1 b) SD3 c) SD4 and d) SD5

## 5.3 Magnetoresistance Measurements

Figure 5.3 shows the raw magnetoresistance measurements of all of the samples with the field parallel to the direction of current flow. By way of comparison, Figure 5.4 shows the raw magnetoresistance measurements of all of the samples with the field perpendicular to the direction of current flow. In all cases the data can been seen to have a low signal to noise ratio at higher temperatures. This is a common problem when performing magnetoresistance measurements [9] and is compensated for by performing such measurements at high fields and lower temperatures [135]. An improved signal to noise ratio is observed in the samples at lower temperatures. However in spite of signal noise issues a prevailing

trend can be observed in the data. In both the case of parallel and perpendicular magnetoresistance a transition from negative to positive magnetoresistance is observed with decreasing temperature.

Four anomalies are present in the data set, the 300 K and 260 K measurements of SD1 and SD4. In the case of SD1, the 300 K measurement first undergoes positive magnetoresistance and at a field of approximately 200 mT reaches a maximum and begins to decrease until a region of negative magnetoresistance is entered which persists for the remainder of the field range studied. The 260 K measurement for SD1 also displays a positive magnetoresistance which in all other samples displayed a negative magnetoresistance. In the case of SD4, the 300 K measurement has a very low signal to noise ratio, almost to the point where no discernible trend can be observed, but it can be seen that the sample starts with a high positive magnetoresistance which continually decreases into a small negative magnetoresistance. The 260 K measurement for SD4 behaves similarly to the 260 K measurement for SD1 and a positive magnetoresistance is observed where otherwise it would be negative.

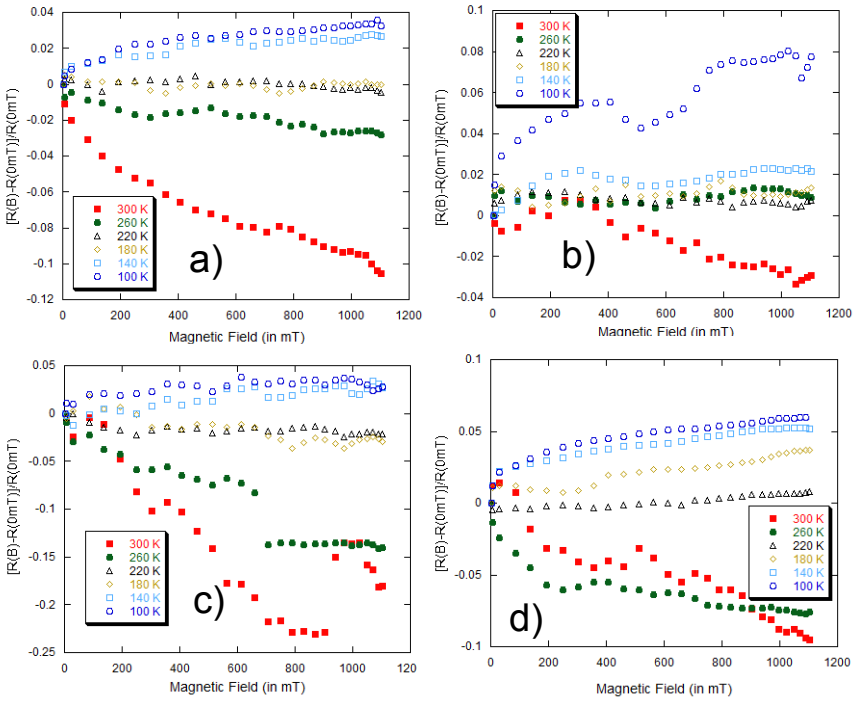


Figure 5.3: Raw magnetoresistance measurements of the samples a) SD1 b) SD3 c) SD4 and d) SD5 with the field parallel to the direction of current flow

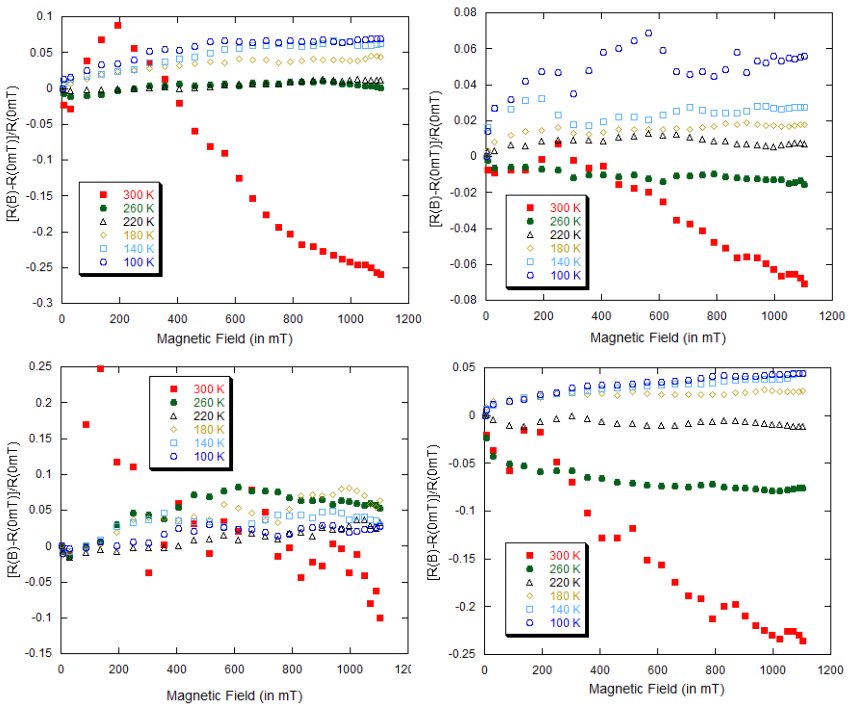


Figure 5.4: Raw magnetoresistance measurements of the samples a) SD1 b) SD3 c) SD4 and d) SD5 with the field perpendicular to the direction of current flow

## 5.4 Resistance Measurements Model Fits

In order to provide a physical interpretation for the observed trends in the experimental results, appropriate models need to be fitted to the data, the most likely candidate selected and the extracted parameters compared with values for similar materials found in the literature. The models previously discussed in the literature review will be used due to the success they have found in describing the transport properties of similar materials. Fits of all three models, Mott VRH, ES-VRH and FIT, were initially applied to the sample SD3 to determine which described the low temperature data best. The sample SD3 was chosen as it has measurements performed down to 10 K, meaning it had data over the largest temperature range.

Figure 5.5 shows the fits of all three models to the SD3 resistance data. All of the models show good correspondence to the data, but it is clear that FIT provides the best description. This is verified by the values of the coefficient of determination ($R^2$) extracted from the fits. FIT displayed the highest $R^2$ value. These values are shown in Table 5.1.

These results would suggest that FIT is the dominant electrical transport mechanism in

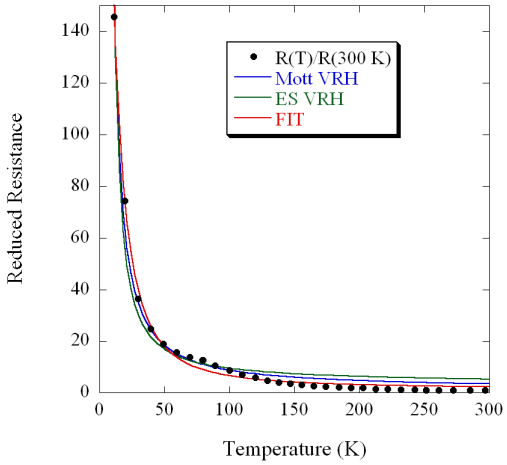


Figure 5.5: Model fits to SD3 resistance data. While all three models provide a credible description of the data, it is clear that fluctuation induced tunnelling provides the best.

| Model | $R^2$ Value |
|---|---|
| Mott VRH | 0.987 |
| ES VRH | 0.967 |
| FIT | 0.996 |

Table 5.1: Values for the coefficient of determination ($R^2$) for the fits of the three models fitted to SD3's resistance data.

this sample. Attemps to fit combinations of the proposed models to the data did not yield better results. Transport measurements on individual spheres are being explored to look at the differences between inter-particle and intra-particle transport. Performing a similar test on the low temperature resistance data of the other samples has shown similar results. This indicates that the semiconducting behaviour can be described best by FIT in all of the samples studied. It is possible that the points of contact at the boundaries of adjacent spheres act as the potential barrier described in FIT models. This model could be applied unaltered to the resistance data of SD1 because SD1 displays only semiconducting behaviour across the temperature range studied like SD3. In the case of SD4 and SD5, the model must be altered to accommodate the observed metallic behaviour. A possible candidate to model the metallic behaviour is a quasi-1 dimensional metallic model based on electron phonon interactions initially explored by Pietronero [136]. This model has been used as an additive term to expressions like those for FIT and Mott VRH to account for the metallic behaviour found in the resistance measurements of CNT ropes [137] and mats [134]. This model should account for the data well as quasi-1 dimensional behaviour has been seen in chains of conducting carbon nanoparticles [86]. The expression for this quasi-1 dimensional metallic behaviour is given by:

$$R(T) = Q \exp\left(-\frac{T_m}{T}\right) \tag{5.1}$$

where $Q$ contains information regarding the geometry of the sample and $T_m$ is the characteristic temperature which when multiplied by the Boltzmann constant gives the energy of phonons across the Fermi surface that will backscatter carriers [137]. The resulting equation fitted to data of the samples displaying a transition from metallic to semiconducting behaviour is given by:

$$R(T) = Q \exp\left(-\frac{T_m}{T}\right) + \beta \exp\left(\frac{T_b}{T_s + T}\right) \tag{5.2}$$

where all symbols used retain the meaning previously described in this dissertation. Figure 5.6 shows the expressions for FIT and FIT modified with the quasi-1 dimensional metallic term fitted to the resistance data of SD1, SD4 and SD5. The parameters extracted from the FIT model fits to the resistance data of all samples are depicted in Table 5.2.

The model fits show excellent correspondence to the data for all of the samples studied. The parameters extracted from the curve fits are consistent with those for nitrogen doped CNT mats, single walled CNT mats and doped polyacetylene found in the lit-

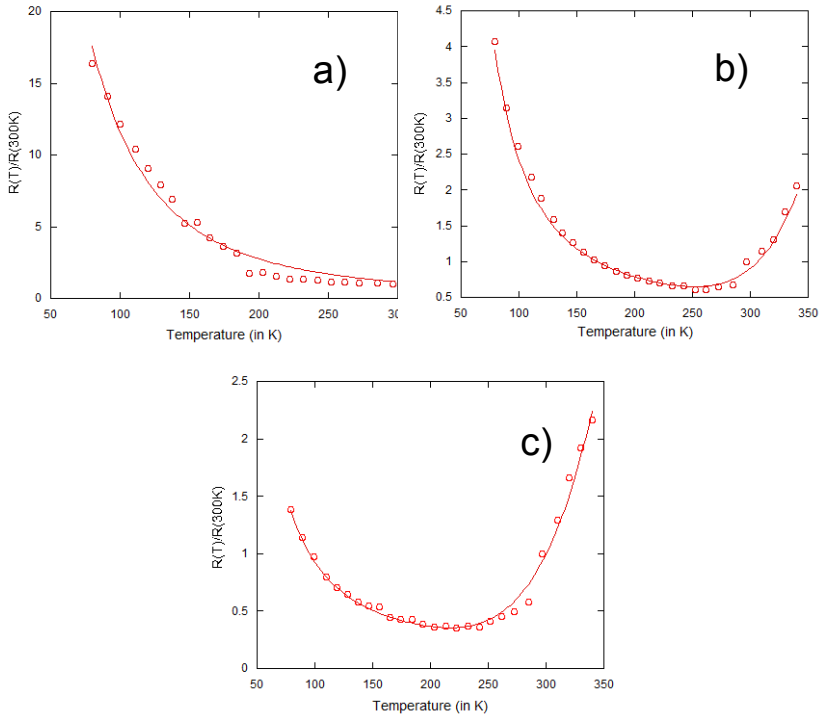


Figure 5.6: Fluctuation induced tunnelling fits to the resistance data of a) SD1 and fluctuation induced tunnelling fits with a quasi-1 dimensional metallic term fits to the resistance data of b) SD4 c) SD5

Table 5.2: Parameters extracted from the fluctuation induced tunnelling model fit to the resistance data of all samples

| Sample | $T_b$ in K | $T_s$ in K | $\beta$ |
|---|---|---|---|
| SD1 | $2000 \pm 1000$ | $200 \pm 99$ | $0.04 \pm 0.06$ |
| SD3 | $250 \pm 30$ | $40 \pm 4$ | $1.2 \pm 0.2$ |
| SD4 | $334 \pm 79$ | $30 \pm 17$ | $0.2 \pm 0.05$ |
| SD5 | $337 \pm 187$ | $44 \pm 40$ | $0.09 \pm 0.05$ |

erature [132], [134], [105]. The large variety of type and number of junctions between interconnecting microparticles has been hypothesised to be the cause of the large uncertainties in the values for $T_s$ and $T_b$ [132]. The spherical nature of the microparticles results in a greater potential for different kinds of contacts to exist between them. In the case of SD3, the experiments performed achieved lower temperatures than the value of $T_s$ extracted from the model fits. This shows that the role thermal fluctuations play in allowing electrons to traverse the barriers between metallic regions is small in this temperature range. A higher barrier height between conducting regions is inferred from the $T_b$ values which are higher than those for nitrogen doped CNTs [132]. The values of $T_s$ and $T_b$ extracted from the fits to the resistance data obtained from SD1 are substantially larger than those of the other samples. Large values such as these have been observed in arrays of fine graphite powders [138].

The values for the characteristic temperature, $T_m$ extracted from the quasi-1 dimensional metallic term in the case of SD4 and SD5 display values that are more than double the value seen in CNT ropes and conducting polymer nanowires [137]. The extracted values were 3362 K ± 443 K for SD4 and 2509 K ± 171 K for SD5. This indicates that much higher energy phonons will result in the backscattering of carriers than in CNT ropes.

## 5.5 IV Characteristics Model Fits

Since the results of the resistance measurements indicate that FIT is the most promising candidate from a mathematical point of view to explain electrical transport of the samples, a model that predicts the trends seen in the IV characteristics of a systems that conducts via FIT is required. One such model was numerically determined by Kaiser [139] and is given by:

$$G = \frac{I}{V} = G_0 \frac{e^{\left(\frac{V}{V_0}\right)}}{1 + h\left(e^{\frac{V}{V_0}} - 1\right)} \tag{5.3}$$

where $G_0$ is the temperature dependent low field conductance, $h$ is the parameter which governs the slowing of exponential increase at higher field values and $V_0$, which has a strong dependence on the potential barrier height, is the voltage scaling factor. In order to achieve the desired behaviour, $h < 1$. This model relates the changing linearity of the IV curves to the ability of electrons to surmount the potential barriers set up between conducting regions [140]. At higher temperatures, electrons are able to move over

Table 5.3: Parameters extracted from the fluctuation induced tunnelling model fit to the IV characteristics of SD1 and SD3. Errors not included due to space limitations.

| Sample | Parameters | 100 K | 140 K | 180 K | 220 K | 260 K | 300 K |
|---|---|---|---|---|---|---|---|
| SD1 | $G_0$ (in mS) | 0.12 | 0.18 | 0.26 | 0.29 | 0.27 | 0.29 |
| | $V_0$ (in V) | 15 | 14 | 10 | 7 | 6 | 18 |
| | $h$ | 0.16 | 0.21 | 0.34 | 0.39 | 0.38 | 0.36 |
| SD3 | $G_0$ (in mS) | 0.15 | 0.26 | 0.41 | 0.51 | 0.55 | 0.55 |
| | $V_0$ (in V) | 26 | 26 | 35 | 37 | 51 | $-67$ |
| | $h$ | 0.001 | 0.114 | 0.245 | 0.36 | 0.36 | 0.87 |

the potential barriers of the non-conducting regions with energy provided from thermal fluctuations. This accounts for near linear IV Characteristics at higher temperatures. At lower temperatures the electrons do not have sufficient energy to surmount the barriers and therefore the electrons tunnel through the barriers, resulting in an increasing nonlinear component in the measurements.

However the model proposed does not explain the saturation behaviour observed in the IV curves. The fact that the saturation behaviour in the IV curves is observed in the same temperature region where metallic behaviour is observed in the resistance measurements indicates that the two phenomena must be related to the same physical mechanism. Taking into account that the quasi-1 dimensional metallic term was derived by considering electron phonon interactions, an expression describing the IV curves of a similar system is desirable. One such model was numerically determined by Yao *et al* [141]. The saturation behaviour observed is related to the emission of optical and zone boundary phonons. This increases the probability of scattering and reduces the energy of the electrons in the case of inelastic scattering resulting in increases in potential creating smaller and smaller increases in current. The expression has been used in studying the electrical break down of CNTs [142]. The expression is given by:

$$R = \frac{V}{I} = R_0 + \frac{V}{I_0} \tag{5.4}$$

where $R_0$ describes low field elastic scattering and $I_0$ is the saturation current.

Figure 5.7 shows fits of the FIT IV characteristics model and the saturation model based on electron phonon interactions to the data. For all samples the models show excellent correspondence to the data. Table 5.3 shows the parameters extracted from the fits to the samples SD1 and SD3 and Table 5.4 shows the parameters extracted from the fits to

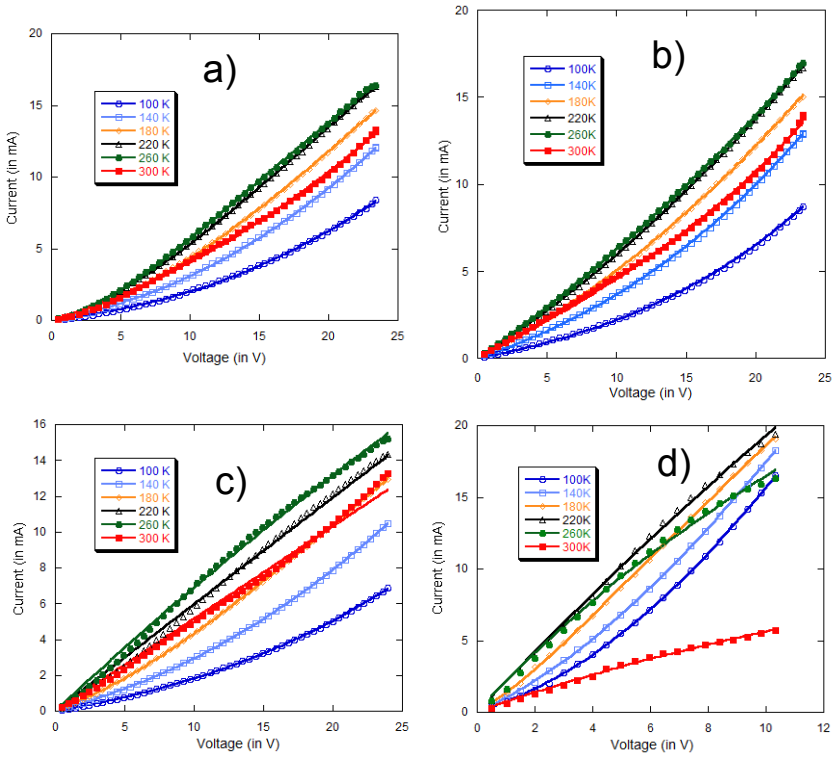


Figure 5.7: Fluctuation induced tunnelling fits to the IV characteristic data of a) SD1 b) SD3 and fluctuation induced tunnelling fits with electron-phonon interaction expression fits to the IV characteristic data of c) SD4 d) SD5

Table 5.4: Parameters extracted from the fluctuation induced tunnelling and electron-phonon interactions model fits to the IV characteristics of SD4 and SD5. Errors not included due to space limitations.

| Sample | Parameters | 100 K | 140 K | 180 K | 220 K | 260 K | 300 K |
|---|---|---|---|---|---|---|---|
| SD4 | $G_0$ (in mS) | 0.13 | 0.21 | 0.3 | | | |
| | $V_0$ (in V) | 29.33 | 22.6 | 10.02 | | | |
| | $h$ | 0.04 | 0.2 | 0.5 | | | |
| | $R_0$ (in kΩ) | | | | 1.56 | 1.38 | 1.85 |
| | $I_0$ (in mA) | | | | 203 | 149 | 168 |
| SD5 | $G_0$ (in mS) | 0.66 | 0.92 | 1.16 | | | |
| | $V_0$ (in V) | 6.16 | 6.35 | 2.32 | | | |
| | $h$ | 0.28 | 0.4 | 0.62 | | | |
| | $R_0$ (in kΩ) | | | | 0.47 | 0.45 | 1.37 |
| | $I_0$ (in mA) | | | | 187 | 65 | 24 |

the samples SD4 and SD5. These extracted parameters show good agreement with those found in the literature for conducting polymer nanowires. Similar trends in these values with changing temperature are also observed [140]. The 300 K data point is shown to be an anomaly specifically in the case of SD3 where the parameters obtained from the fits to the data do not follow the same pattern as the other higher temperature measurements and in the case of the voltage scale factor $V_0$ a non-physical negative value was obtained. The origin of this anomaly could be further explored by performing IV characteristics measurements at higher temperatures to see if the data continues to follow this trend. The fact that FIT shows good correspondence to both the resistance and IV data in the same temperature ranges provides a good argument that this is the dominant conduction mechanism in these samples.

Similarly the model of Yao *et al* provides a good description of the high temperature data in SD4 and SD5 as shown by the good fits to the experimental data. In all cases, the value of the saturation current $I_0$ is much higher than those obtained for individual single walled CNTs. For individual single walled CNTs, $I_0$ was determined to be 25 $\mu$A [141]. This difference can be attributed to the bulk nature of the samples studied in this research because bundles of single walled CNTs have been shown to have a much higher saturation current than individual single walled CNTs [142].

## 5.6 Magnetoresistance Model Fits

Unlike materials where Mott VRH [143] or weak localization [70] are determined to be dominant conduction mechanisms, there is no well-defined theoretical description of the magnetoresistance behaviour of a material that conducts via FIT [72]. Experimental observations have been made of both positive and negative magnetoresistance in systems where FIT is determined to be the dominant conduction mechanism [138], [144]. These observations were described in the context of other transport regimes in the case of arrays of fine graphite powders [138]. In this case negative magnetoresistance was explained using level crossing and shifting due to magnetic fields while positive magnetoresistance was described in terms of electron wave function shrinkage. In the case of polymer-amorphous carbon composite networks, only negative magnetoresistance was observed and this was attributed to electron-electron interactions [144].

Drawing a comparison between the results obtained in this research and the results obtained by others is difficult as different field and temperature ranges were studied in each separate case. Pakhomov *et al* did perform higher temperature measurements but

at much higher fields and so the details of low field behaviour cannot be seen in their measurements [138]. At high fields and high temperatures (300 K) a positive magnetoresistance is observed which differs to the results obtained in this research where negative magnetoresistance is observed. However, this difference could be connected to the anomalous behaviour observed at 300 K as evidenced by the IV characteristics. Positive magenotoresistance is observed at 150 K which corresponds to the data obtained at 140 K for all samples in this research. At lower temperatures (40 K) a transition to negative magnetoresistance was observed by Pakhomov *et al*. These temperatures were not explored in this research. Pakhomov *et al* found the magnetoresistance to have a quadratic dependence on the field in the positive magnetoresistance regime. Because the 140 K measurement is the only point where a comparison can be drawn, the 140 K measurement for each sample will be fitted with an equation of the form:

$$\frac{\Delta\rho}{\rho_0} = a_+ B^2 - a_- B \tag{5.5}$$

where $a_+$ is a fitting parameter to account for the observed positive magnetoresistance with a quadratic dependence and $a_-$ is a fitting parameter to account for the observed negative magnetoresistance with a linear field dependence. These fits will help determine if a similar physical mechanism is behind the observed data in this research. Figure 5.8 shows the fits of this equation to the 140 K magnetoresistance measurement of all the samples with the field orientated both parallel and perpendicular to the direction of current flow. Fits of the equation to the data are poor. In many cases the fits do not even approximate the trends in the data and due to the simplistic nature of the model there is no leeway to experiment with the initial parameters in the fitting routines used to obtain a better fit. This shows that relating the data obtained in this research to those obtained elsewhere [138], [144] is not feasible and leaves the results of these experiments inconclusive. However this does not mean that the data obtained from these magnetoresistance experiments are the result of an error as the explanations of the data obtained by Pakhomov *et al* and Prasad *et al* were based on other transport mechanisms. Once a model of magnetoresistance in materials which conduct via FIT has been derived, this experimental data can be revisited.

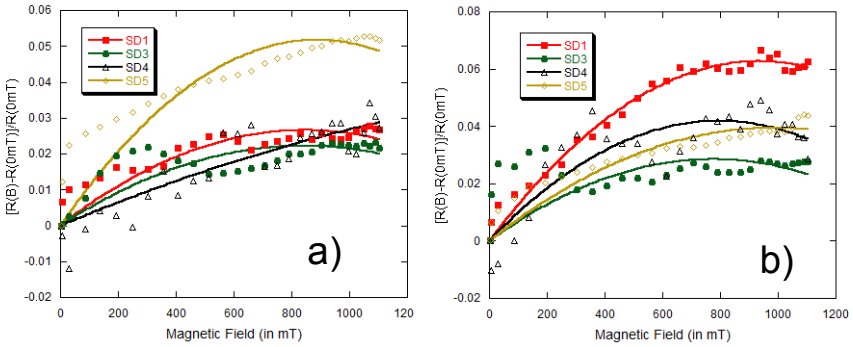


Figure 5.8: Fits of Equation 5.5 to the 140 K magnetoresistance measurements of all samples with the field orientated a) parallel to the direction of current flow and b) perpendicular to the direction of current flow

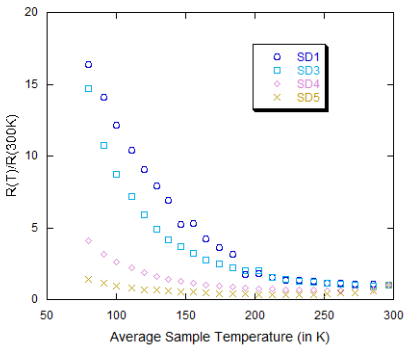


Figure 5.9: Comparison between the resistance measurements of all samples in the temperature range 300 K - 80 K to determine the effect of nitrogen doping on the conductivity of carbon microspheres

## 5.7 Effect of Nitrogen doping on Transport in Carbon Microspheres

Figure 5.9 shows the resistance data of all samples over the temperature range 300 K to 80 K. This is to compare the resistance data of all the samples so that conclusions regarding the effect of nitrogen doping on electrical transport in CMSs can be drawn. All of the resistance data have been normalized to the resistance obtained at 300 K so that comparisons between different samples can be made.

According to these comparisons, the effect of nitrogen doping on electrical transport in CMSs is inconclusive and a pattern cannot be discerned from the data. This can be seen in the fact that SD1 has a nitrogen concentration of 1.7 %, identical to SD5, but SD1 has the largest temperature variation in resistance and SD5 has the lowest. The two also display unique characteristics, SD5 displaying metallic behaviour at higher temperatures whereas SD1 does not. The same is true for the samples SD3 and SD4. They both have the same nitrogen concentration of 3.4 % but display different trends in their resistance data.

Taking into account that samples were collected from varying points in the reactor, this result points out that the changes in synthesis parameters have a drastic effect on the conductive properties of the samples and before any definite comments can be made regarding the effect of doping, samples must be synthesized under defined conditions. These results could be refined by performing resistivity measurements to remove the effects of sample geometry from the measurements.

## 5.8 Effect of Atmospheric doping on Transport in Carbon Microspheres

Previous studies have shown that the surrounding environment can have a large impact on the electrical properties of carbon nanomaterials. Semiconducting CNT mats have been shown to change their conductive properties from p-type to n-type with increases in the water vapour content of the surrounding atmosphere. It was hypothesised by Zahab *et al* that the water molecules act as electron donors [145]. Oxygen has also been shown to influence the transport properties of CNTs by causing semiconducting nanotubes to behave as metallic nanotubes [146]. These reports inspired the study of the electrical transport properties of the two samples that did not display metallic properties a year

later to see if any effect on the transport properties could be found.

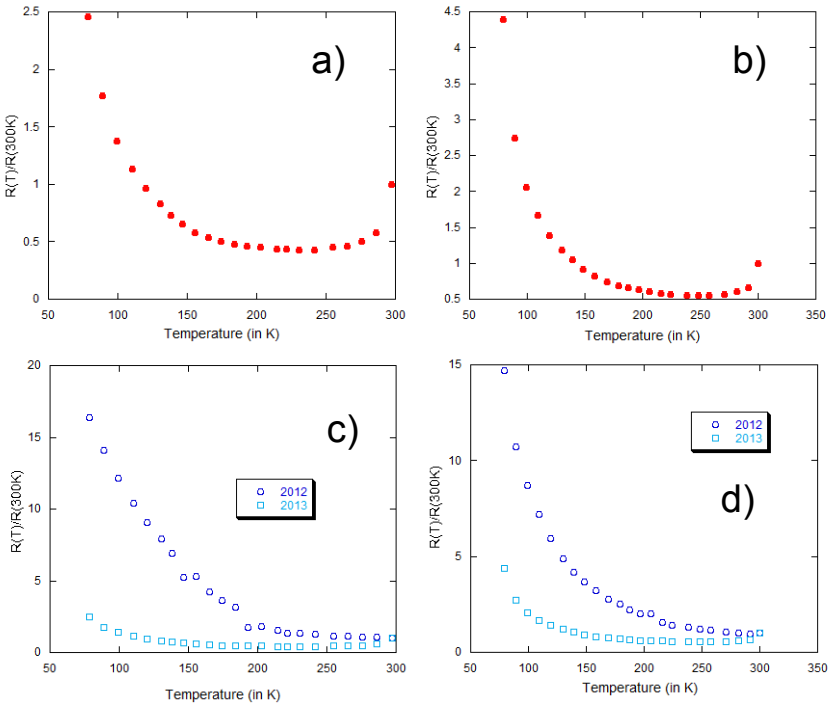


Figure 5.10: Resistance measurements of the samples a) SD1 and b) SD3 performed a year after the initial experiments were performed to investigate the effect of atmospheric doping. Comparisons between the initial data and the data taken a year later for c) SD1 and d) SD3

Figure 5.10 shows the resistance measurements of the samples SD1 and SD3 a year after the initial experiments were performed. A similar transition to metallic behaviour is now observed in the samples where previously there was none. A comparison between the data taken initially and one year later is also shown in Figure 5.10 and shows a decrease in the temperature dependence of the resistivity. This new transition from semiconducting behaviour to metallic behaviour and a reduction in resistivity are indicators that the samples could have been atmospherically doped with oxygen and water vapour as seen in previous work [145], [146]. To determine exactly which would require more in-depth analysis. This doping could have occurred during general handling of the sample as the sample was never kept in a vacuum environment. While changes in atmosphere have shown to result in quick changes in electrical properties of individual CNTs [146], the fact that it took a year for such effects to be noticed could be ascribed to the bulk nature of the samples studied in this research.

Figure 5.11 shows the fits of the FIT model modified with the quasi 1-dimensional metallic term as used previously to the data. This is to show that the same conduction mechanisms as still at work in the samples. The fits show excellent correspondence with the data. Heat

treatment experiments will be performed to test the hypothesis of atmospheric doping further.

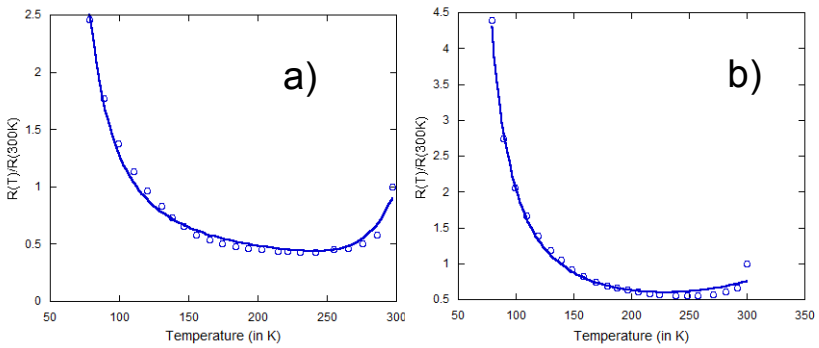


Figure 5.11: Fits of the FIT model modified with the quasi-1 dimensional metallic term to the resistance data of the samples a) SD1 and b) SD3 obtained a year after initial measurements were taken. The fits show excellent correspondence to the data showing the same conduction mechanisms are at work.

# 6 Conclusions

This chapter will summarize the results of this research and provide suggestions for future work to further expand on the results obtained.

## 6.1 Summary

A suite of four samples of n-CMSs, each sample containing a different level of nitrogen dopant, was synthesised using a h-CVD technique without the use of a catalyst. The samples were given the arbitrary designations SD1, SD3, SD4 and SD5. The samples were characterized using SEM, Raman spectroscopy and EPR spectroscopy. SEM confirmed the spherical nature of the nanomaterials formed and allowed for the average diameters of the spheres synthesized to be determined. This was in the micrometer range so the spheres can be deemed microspheres. Raman spectroscopy confirmed the graphitic nature of the samples synthesized determining that the microspheres were in fact composed of carbon. EPR spectroscopy showed a strong paramagnetic signal which is indicative of the nitrogen incorporation into the graphitic lattice. EPR spectroscopy was also used as a non-destructive technique to determine the amount of nitrogen included in the samples.

Electrical transport measurements were performed on all samples. To achieve this, an electrical transport station was designed and built in the laboratory. This station included all the necessary experimental apparatus which were interfaced with a computer. Software was written to allow for the electrical transport measurements to be automated. Resistance measurements showed that SD1 and SD3 displayed purely semiconducting behaviour across the entire temperature range studied while SD4 and SD5 displayed semiconducting behaviour at low temperatures and experienced a transition to metallic behaviour at higher temperatures. This characteristic 'U-shape' has been widely reported on in the literature and has been ascribed to the thermal desorption of nitrogen dopant. The IV Characteristics of SD1 and SD3 displayed a distinct trend in the linearity of the data. High temperature measurements displayed a strong linear component and as the temperature was decreased, the data became more non-linear. The 300 K data point was

anomalous in that it had a strong non-linear component, but the non-linear behaviour did not fit that of the lower temperature data. SD4 and SD5 displayed a similar progression from linearly dominated IV characteristics to non-linearly dominated IV characteristics at lower temperatures but at higher temperatures saturation behaviour was observed. The temperature range over which this behaviour was observed corresponded with the temperature range where metallic behaviour was observed in the resistance measurements. The 300 K data point was anomalous in that the measured currents were much lower than other high temperature measurements. The magnetoresistance measurements with the direction of current flow oriented both parallel and perpendicular to the field showed a general transition from positive to negative magnetoresistance across the sample suit.

Attempts to fit common models of conduction in disordered semiconductors to the resistance data were made. These models were Mott VRH, ES-VRH and FIT. While all the models provided a credible explanation for the results, by comparing the quality of the different fits to the data it was determined that FIT provided the best description of the semiconducting behaviour in all samples. The parameters extracted from these fits showed good correspondence with those seen in the literature. In order to account for the metallic behaviour observed in SD4 and SD5, a commonly used, additive, quasi-1 dimensional metallic term was fitted to the data. This fit showed good correspondence to the data and the extracted parameters compared well with those found in the literature. To account for the trends seen in the IV characteristics, a numerically derived model describing the IV characteristics of a system that conducts via FIT was fitted to the semiconducting data. This model showed excellent correspondence to the data and the parameters extracted compared excellently with those found in the literature. In order to account for the saturation behaviour a model based on electron-phonon interactions was used and when fitted to the data excellent correspondence was obtained. The magnetoresistance data proved very difficult to model as a theoretical description of a system that conducts via FIT has yet to be derived. Comparisons were made to existing experimental observations for the magnetoresistance of such systems and few similarities were found. In the cases where similarities were found, models were fitted to the data, but poor correspondence was obtained. However this is not yet evidence of error in the data as the models used were derived from other conduction mechanisms such as weak localization and may not be applicable to FIT.

The resistance measurements of all samples across a common temperature range were compared in order to determine the effect of nitrogen doping across the samples. The results of this comparison are inconclusive as samples with identical nitrogen content displayed very different transport properties. The comparison could be made more effective by ensuring stricter synthesis conditions and performing resistivity experiments to

remove the effects of sample geometry on the results.

Finally a set of resistance measurements were performed on the samples SD1 and SD3 one year after the original experiments were performed in order to determine if any atmospheric doping had occurred in the samples. It was found that the resistance measurements of the samples now displayed a transition to metallic behaviour at higher temperatures and a much lower resistance than was previously observed. Both of these changes are suggestive of doping by water vapour and oxygen. Further experimentation is required to confirm these results.

## 6.2 Future work

Some future work that could be pursued to further the knowledge of the samples includes:

- Higher temperature IV characteristics experiments to gain further insight into the anomalous 300 K data point
- Resistivity measurements to allow for the effects of sample geometry to be disregarded and more accurate comparison between samples made
- Angle dependent magnetoresistance measurements to obtain more insight into the effect magnetic fields have on conduction
- Hall measurements to determine the majority carrier species
- Resistance measurements could be taken at much higher temperatures to investigate the effect of dopant desorption
- CHN analysis could also be used to provide more insight into dopant desorption and confirm the nitrogen content measurements obtained from EPR spectroscopy
- Theoretical work could be undertaken to determine the magnetoresistance of a material that conducts via FIT to obtain a more accurate interpretation of the magnetoresistance data

# References


[1] A. Deshmukh, S. Mhlanga, and N. Coville. *Mat. Sci. Eng. R*, 70:1–28, 2010.

[2] Z. Wang and Z. Kang. *J. Phys. Chem.*, 100:17725–17731, 1996.

[3] Z. Wang and Z. Kang. *J. Phys. Chem.*, 100:5163–5165, 1996.

[4] X. He, F. Wu, and M. Zheng. *Diam. Relat. Mat.*, 16:311–315, 2007.

[5] F. Su, X. Zhao, Y. Wang, L. Wang, and J. Lee. *J. Mater. Chem.*, 16:4413–4419, 2006.

[6] J. Charlier, X. Blase, and S. Roche. *Rev. Mod. Phys.*, 79:667–711, 2007.

[7] K. Mondal, A. Strydom, Z. Tetana, S. Mhlanga, M. Witcomb, J. Havel, R. Erasmus R, and N. Coville. *Mat. Chem. Phys.*, 114:973–977, 2009.

[8] N. Kunjuzwa. N-doping of the carbon spheres and the synthesis of polythiophene/carbon sphere composites. Master's Dissertation, 2009.

[9] C. Kasl. Electric Transport Investigations on the Trivalent-Ion Doped Tungsten Bronzes Near the Metal-Insulator Transition. Ph.D. Thesis, University of the Witwatersrand.

[10] S. Iijima. *Nature*, 354:56–58, 1991.

[11] H. Kroto, J. Heath, S. OBrien, R. Curl, and R. Smalley. *Nature*, 318:162–163, 1985.

[12] S. Baker, K. Tse, C. Lee, and R. Hamers. *Diam. Rel. Mat.*, 15:433–439, 2006.

[13] H. Wang, M. Chhowalla, N. Sano, S. Jia, and G. Amaratunga. *Nanotech.*, 15:546–550, 2004.

[14] N. Katcho, P. Zetterstrom, E. Lomba, J. Marco, E. Urones-Garrote, D. Avila-Brande, and A. Gomez-Herrero. *Phys. Rev. B*, 77:195402, 2008.

[15] M. Terrones. *Annu. Rev. Mater. Res.*, 33:419–501, 2003.

[16] E. Rakov. *Russ. Chem. Rev*, 70:827–863, 2001.

[17] M. Endo, T. Hayashi, Y. Kim, M. Terrones, and M. Dresselhaus. *Phil. Trans. R. Soc. Lond. A*, 362:2223–2238, 2004.

[18] E. Dannenberg. *Rubb. Chem. Tech.*, 59:512–524, 1986.

[19] J. Belmont, J. Johnson, and C. Adams. Ink jet ink formulations containing carbon black products, 11 1996.

[20] R. Dominko, M. Gaberscek, J. Drofenik, M. Bele, S. Pejovnik, and J. Jamnik. *J. Pow. Sour.*, 119:770–773, 2003.

[21] S. Pol, V. Pol, D. Sherman, and A. Gedanken. *Green Chem.*, 11:448–451, 2009.

[22] Y. Xia, B. Gates, Y. Yin, and Y. Lu. *Adv. Mat*, 12:693–713, 2000.

[23] M. Inagaki. *Carbon*, 35:711–713, 1997.

[24] P. Serp, R. Feurer, P. Kalck, Y. Kihn, J. Faria, and J. Figueiredo. *Carbon*, 39:621–626, 2001.

[25] V. Pol, S. Pol, A. Gedanken, M. Sung, and S. Asai. *Carbon*, 42:2738–2741, 2004.

[26] R. Shaddix and T. Williams. *Am. Sci.*, 95:232, 2007.

[27] Z. Wang and Z. Kang. *Philos. Mag. B*, 73:905–929, 1996.

[28] T. Ebbesen and P Ajayan. *Nature*, 358:220–222, 1992.

[29] J. Qiu, Y. Li, Y. Wang, C. Liang, T. Wang, and D. Wang. *Carbon*, 41:767–772, 2003.

[30] S. Kim, E. Shibata, R. Sergiienko, and T. Nakamura. *Carbon*, 46:1523–1529, 2008.

[31] Y. Ma, Z. Hu, K. Huo, Y. Lu, Y. Hu, Y. Liu, J. Hu, and Y. Chen. *Carbon*, 43:1667–1672, 2005.

[32] H. Qian, F. Han, B. Zhang, Y. Guo, J. Yue, and B. Peng. *Carbon*, 42:761–766, 2004.

[33] M. Aili, W. Xiaomin, L. Tianbao, L. Xuguang, and X. Bingshe. *Mat. Sci. Eng. A*, 443:54–59, 2007.

[34] V. Pol, M. Motiei, A. Gedanken, J. Calderon-Moreno, and M. Yoshimura. *Carbon*, 42:111–116, 2004.

[35] N. Rodriguez. *J. Mater. Res*, 8:3233–3250, 1993.

[36] M. Sobkowicz, J. Dorgan, K. Gneshin, A. Herring, and J. McKinnon. *Carbon*, 47:622–629, 2009.

[37] T. Thome, J. Colaux, J. Colomer, G. Bertoni, and G. Terwagne. *Mat. Chem. Phys*, 103:290–294, 2007.

[38] Y. Jin, Y. Kim, C. Gao, Y. Zhu, A. Huczko, M. Endo, and H. Kroto. *Carbon*, 44:724–729, 2006.

[39] H. Palmer, A. Voet, and J. Lahaye. *Carbon*, 6:65–70, 1968.

[40] P. Libby and T. Blake. *Combust. Flame*, 36:139–169, 1979.

[41] J. Miao, D. Hwang, K. Narasimhulu, P. Lin, Y. Chen, S. Lin, and L. Hwang. *Carbon*, 42:813–822, 2004.

[42] Y. Jin, C. Gao, W. Hsu, Y. Zhu, A. Huczko, M. Bystrzejewski, M. Roe, C. Lee, S. Acquah, H. Kroto, and D. Walton. *Carbon*, 43:1944–1953, 2005.

[43] M. Sharon, K. Mukhopadhyay, K. Yase, S. Iijima, Y. Ando, and X. Zhao. *Carbon*, 36:507–511, 1998.

[44] R. Alcantara, F. Madrigal, P. Lavela, J. Tirado, J. Mateos, C. Gomez de Salazar, R. Stoyanova, and E. Zhecheva. *Carbon*, 38:1031–1041, 2000.

[45] F. Zhang and H. Li. *Mater. Chem. Phys.*, 98:456–458, 2006.

[46] S. Han, Y. Yun, K. Park, Y. Sung, and T. Hyeon. *Adv. Mat.*, 15:1922–1925, 2003.

[47] J. Kim, B. Fang, M. Kim, and J. Yu. *Catal. Today*, 146:25–30, 2009.

[48] W. Li, D. Chen, Z. Li, Y. Shi, Y. Wan, J. Huang, J. Yang, D. Zhao, and Z. Jiang. *Electrochem. Commun.*, 9:569–573, 2007.

[49] A. Levesque, V. Binh, V. Semet, D. Guillot, R. Fillit, M. Brookes, and T. Nguyen. *Thin Solid Films*, 464-465:308–314, 2004.

[50] L. Nyemba. Reinforcement of synthetic rubber with carbon nanoballs to produce nanocomposite ion exchange membrane. Master's Dissertation, University of the Witwatersrand, 2010.

[51] Y. Song, G. Zhai, G. Li, J. Shi, Q. Guo, and L. Liu. *Carbon*, 42:1427–1433, 2004.

[52] E. Auer, A. Freund, J. Pietsch, and T. Tacke. *Appl. Catal. A*, 173:259–271, 1998.

[53] K. Mondal, L. Cele, M. Witcomb, and N. Coville. *Catal. Commun.*, 9:494–498, 2008.

[54] H. Yoon, S. Ko, and J. Jang. *Chem. Commun.*, 43:1468–1470, 2007.

[55] N. Ballav, A. Maity, and M. Biswas. *Mater. Chem. Phys.*, 87:120–126, 2004.

[56] Z. Liu, J. Park, S. Abdi, S. Park, Y. Park, and W. Lee. *Top. Catal.*, 39:221–226, 2006.

[57] M. Dresselhaus, G. Dresselhaus, and A. Jorio. *Annu. Rev. Mater. Res.*, 34:247–278, 2004.

[58] T. Odom, J. Huang, P. Kim, and C. Lieber. *Lett. Nature*, 391:62–64, 1998.

[59] M. Ouyang, J. Huang, C. Cheung, and C. Lieber. *Science*, 292:702–705, 2001.

[60] M. Ouyang, J. Huang, and C. Lieber. *Acc. Chem. Res.*, 35:1018–1025, 2002.

[61] A. Javey, J. Guo, Q. Wang, M. Lundstrom, and H. Dai. *Lett. Nature*, 424:654–657, 2003.

[62] A. Bachtold, M. Fuhrer, S. Plyasunov, M. Forero, E. Anderson, A. Zettl, and P. McEuen. *Phys. Rev. Lett.*, 84:6082–6085, 2000.

[63] R. Lee, H. Kim, J. Fischer, A. Thess, and R. Smalley. *Lett. Nature*, 388:255–257, 1997.

[64] J. Park, S. Rosenblatt, Y. Yaish, V. Sazonova, H. Ustunel, S. Braig, T. Arias, P. Brouwer, and P. McEuen. *Nano Lett.*, 4:517–520, 2004.

[65] Z. Yao, C. Kane, and C. Dekker. *Phys. Rev. Lett.*, 84:2941–2944, 2000.

[66] A. Bachtold, C. Strunk, J. Salvetat, J. Bonard, L. Forró, T. Nussbaumer, and C. Schönenberger. *Nature Lett.*, 397:673–675, 1999.

[67] C. Schönenberger, A. Bachtold, C. Strunk, J. Salvetat, and L. Forró. *Appl. Phys. A*, 69:283–295, 1999.

[68] V. Skákalová, A. Kaiser, Z. Osváth, G. Vértesy, L. Biró, and S. Roth. *Appl. Phys. A*, 90:597–602, 2008.

[69] Z. Han and K. Ostrikov. *Appl. Phys. Lett.*, 96:233115, 2010.

[70] J. Vavro, J. Kikkawa, and J. Fischer. *Phys. Rev. B*, 71:155410, 2005.

[71] J. Fischer, H. Dai, A. Thess, R. Lee, N. Hanjani, D. Dehaas, and R. Smalley. *Phys. Rev. B*, 55:R4921–R4924, 1997.

[72] V. Ksenevich, V. Odzaev, Z. Martunas, D. Seliuta, G. Valusis, J. Galibert, A. Melnikov, A. Wieck, D. Novitski, M. Kozlov, and V. Samuilov. *J. Appl. Phys.*, 104:073724, 2008.

[73] M. Jaiswal, W. Wang, K. Fernando, Y. Sun, and R. Menon. *Phys. Rev. B*, 76:113401, 2007.

[74] M. Fuhrer, M. Cohen, A. Zettl, and V. Crespi. *Sol. Stat. Comm.*, 109:105–109, 1999.

[75] M. Purewal, B. Hong, A. Ravi, B. Chandra, J. Hone, and P. Kim. *Phys. Rev. Lett.*, 98:186808, 2007.

[76] P. Avouris. *Chem. Phys*, 281:429–445, 2002.

[77] C. Schönenberger. *Semicond. Sci. Technol.*, 21:S1–S9, 2006.

[78] J. Nygard, D. Cobden, M. Bockrath, P. McEuen, and P. Lindelof. *Appl. Phys. A*, 69:297–304, 1999.

[79] A. Javey, M. Shim, and H. Dai. *Appl. Phys. Lett.*, 80:1064–1066, 2002.

[80] Z. Chen, J. Appenzeller, J. Knoch, Y. Lin, and P. Avouris. *Nano Lett.*, 5:1497–1502, 2005.

[81] M. Bockrath, D. Cobden, P. McEuen, N. Chopra, A. Zettl, A. Thess, and R. Smalley. *Science*, 275:1922–1925, 1997.

[82] A. Kasumov, R. Deblock, M. Kociak, B. Reulet, H. Bouchiat, I. Khodos, Y. Gorbatov, V. Volkov, C. Journet, and M. Burghard. *Science*, 284:1508–1511, 1999.

[83] A. Romanenko, O. Anikeeva, A. Okotrub, L. Bulusheva, V. Kuznetsov, Yu. Butenko, A. Chuvilin, C. Dong, and Y. Ni. *Phys. Sol. Stat.*, 44:487–489, 2002.

[84] V. Sandu, G. Aldica, S. Popa, P. Badica, E. Cimpoiasu, F. Dumitrache, and E. Sandu. *J. Appl. Phys*, 110:123921, 2011.

[85] V. Pol. *Environ. Sci. Technol.*, 44:4753–4759, 2010.

[86] A. Bezryadin, R. Westervelt, and M. Tinkham. *Appl. Phys. Lett.*, 74:2699–2701, 1999.

[87] M. Heaney. *Physica A*, 241:296–300, 1997.

[88] J. Macutkevic, P. Kuzhir, A. Paddubskaya, S. Maksimenko, J. Banys, A. Celzard, V. Fierro, S. Bistarelli, A. Cataldo, F. Micciulla, and S. Bellucci. *J. Appl. Phys.*, 114:033707, 2013.

[89] L. El Mir, S. Kraiem, M. Bengagi, E. Elaloui, A. Ouederni, and S. Alaya. *Physica B*, 395:104–110, 2007.

[90] D. van der Putten, J. Moonen, H. Brom, J. Brokken-Zijp, and M. Michels. *Phys. Rev. Lett.*, 69:494–497, 1992.

[91] M. Connor, S. Roy, T. Ezquerra, and F. Calleja. *Phys. Rev. B*, 57:2286–2294, 1998.

[92] P. Mandal, A. Neumann, A. Jansen, and P. Wyder. *Phys. Rev. B*, 55:452–456, 1997.

[93] J. Macutkevic, R. Adomavicius, A. Krotkus, J. Banys, V. Kuznetsov, S. Moseenkov, A. Romanenko, and O. Shenderova. *J. Appl. Phys.*, 111:103701, 2012.

[94] J. Sánchez-González, A. Macías-García, M. Alexandre-Franco, and V. Gómez-Serrano. *Carbon*, 43:741–747, 2005.

[95] F. Li, Q. Zou, and Y. Xia. *J. Pow. Sou.*, 177:546–552, 2008.

[96] M. Nishizawa, H. Koshika, R. Hashitani, T. Itoh, T. Abe, and I. Uchida. *J. Phys. Chem. B*, 103:4933–4936, 1999.

[97] S. Yang, X. Feng, L. Zhi, Q. Cao, J. Maier, and K. Mullen. *Adv. Mater.*, 22:838–842, 2010.

[98] J. Liu and D. Xue. *Nanoscale Res. Lett.*, 5:1525–1534, 2010.

[99] H. Kim, M. Fortunato, H. Xu, J. Bang, and K. Suslick. *J. Phys. Chem. C*, 115:20481–20486, 2011.

[100] F. Su, C. Poh, J. Chen, G. Xu, D. Wang, Q. Li, J. Lin, and X. Lou. *Energy Environ. Sci.*, 4:717–724, 2011.

[101] B. Last and D. Thouless. *Phys. Rev. Lett.*, 27:1719–1721, 1971.

[102] S. Washburn and R. Webb. *Rep. Prog. Phys.*, 55:1311–1383, 1992.

[103] N. Mott. *Metal-Insulator Transitions*. Taylor and Francis, London, UK, 1974.

[104] A. Efros and B. Shklovskii. *J. Phys. C*, 8:L49–L51, 1975.

[105] P. Sheng. *Phys. Rev. B*, 21:2180–2195, 1980.

[106] Z. Wang and J. Yin. *Chem. Phys. Lett.*, 289:189–192, 1998.

[107] Z. Mehraban, F. Farzaneh, and V. Dadmehr. *Mat. Lett.*, 63:1653–1655, 2009.

[108] H. Wu, C. Hong, H. Chiu, and Y. Li. *Diam. Rel. Mat.*, 18:601–605, 2009.

[109] R. Andrews, D. Jacques, D. Qian, and T. Rantell. *Acc. Chem. Res.*, 35:1008–1017, 2002.

[110] A. Jones and M. Hitchman. *Chemical vapour deposition: precursors, processes and applications*. Royal Society of Chemistry, London, UK, 2009.

[111] D. Dobkin and M. Zuraw. *Principles of Chemical Vapor Deposition*. Kluwer Academic Publishers, AH Dordrecht, The Netherlands, 2003.

[112] M. Bystrzejewski, H. Lange, A. Huczko, P. Baranowski, H. Hubers, T. Gemming, T. Pichler, B. Buchner, and M. Rummeli. *J. Sol. Stat. Chem.*, 181:2796–2803, 2008.

[113] R. Caudillo, X. Gao, R. Escudero, M. Jos-Yacaman, and J. Goodenough. *Phys. Rev. B*, 74:214418, 2006.

[114] H. Hou, A. Schaper, F. Weller, and A. Greiner. *Chem. Mater.*, 14:3990–3994, 2002.

[115] K. Smith and C. Oatley. *Br. J. Appl. Phys.*, 6:391–399, 2008.

[116] M. Amer, M. El-Ashry, and J. Maguire. *J. Chem. Phys.*, 121:2752–2757, 2004.

[117] N. Ferrer-Anglada, A. Monge, and S. Roth. *Phys. Status Solidi B*, 247:2823–2826, 2010.

[118] D. Long. *Raman Spectroscopy*. McGraw Hill International Book Company, Maidenhead, UK, 1977.

[119] F. Tuinstra and J. Koenig. *J. Chem. Phys.*, 53:1126, 1970.

[120] M. Pimenta, G. Dresselhaus, M. Dresselhaus, L. Canado, A. Jorio, and R. Saito. *Phys. Chem. Chem. Phys.*, 9:1276–1291, 2007.

[121] D. Yuan, J. Chen, J. Zeng, and S. Tan. *Electrochem. Com.*, 10:1067–1070, 2008.

[122] B. Corzilius, K. Dinse, and K. Hata. *Phys. Chem. Chem. Phys.*, 9:6063–6072, 2007.

[123] M. Galambos, G. Fábián, and F. Simon *et al. Phys. Status Solidi B*, 246:2760–2763, 2009.

[124] J. Weil. and J. Bolton. *Electron Paramagnetic Resonance: Elementary Theory and Practical Applications*. Wiley, New York, USA, 2007.

[125] F. Dyson. *Phys. Rev.*, 98:349–359, 1955.

[126] K. Mondal, A. Strydom, R. Erasmus, J. Keartland, and N. Coville. *Mat. Chem. Phys.*, 111:386–390, 2008.

[127] W. Hsu, S. Chu, and E. Muñoz-Picone *et al. Chem. Phys. Lett.*, 323:572–579, 2000.

[128] J. Keartland, M. Dubazane, V. Marsicano, N. Kunjuzwa, and N. Coville. *Proceedings of SAIP Conference 2011*, 56:127–133, 2011. ISBN: 978-1-86888-688-3.

[129] C. Kasl and M. Hoch. *Rev. Sci. Instrum.*, 76:33907, 2005.

[130] J. Singleton. *Band Theory and Electronic Properties of Solids*. Oxford, New York, USA, 2004.

[131] A. Kaiser. *Rep. Prog. Phys.*, 64:1–49, 2001.

[132] T. Barnes, J. Blackburn, J. Lagemaat, T. Coutts, , and M. Heben. *ACS. Nano.*, 2:1968–1976, 2008.

[133] A. Kaiser, G. Dusberg, and S. Roth. *Phys. Rev. B*, 57:1418–1421, 1998.

[134] M. Shiraishi and M. Ata. *Synth. Metal.*, 128:235–239, 2002.

[135] P. Choudhury, M. Jaiswal, and R. Menon. *Phys. Rev. B*, 76:235432, 2007.

[136] L. Pietronero. *Synth. Met.*, 8:225–231, 1983.

[137] A. Kaiser, G. McIntosh, K. Edgar, J. Spencer, H. Yu, and Y. Park. *Curr. Appl. Phys.*, 1:50–55, 2001.

[138] A. Pakhomov, X. Zhang, H. Liu, X. Wang, H. Huang, and S. Yang. *Physica B*, 279:41–44, 2000.

[139] A. Kaiser, S. Rogers, and Y Park. *Mole. Crys. Liq. Crys.*, 415:115–124, 2004.

[140] Y. Long, Z. Yin, M. Li, C. Gu, J. Duvail, A. Jin, and M. Wan. *Chinese. Phys. B*, 18:2514–2522, 2009.

[141] Z. Yao, C. Kane, and C. Dekker. *Phys. Rev. Lett.*, 84:2941–2944, 2000.

[142] M. Radosavljevic, J. Lefebvre, and A. Johnson. *Phys. Rev. B*, 64:241307, 2001.

[143] G. Kim, E. Choi, D. Kim, D. Suh, and Y. Park. *Phys. Rev. B*, 58:16064–16069, 1998.

[144] S. Shekhar, V. Prasad, and S. Subramanyam. *Phys. Lett. A*, 361:500–503, 2007.

[145] A. Zahab, L. Spina, P. Poncharal, and C. Marliere. *Phys. Rev. B*, 62:10000–10003, 2000.

[146] P. Collins, K. Bradley, M. Ishigami, and A. Zettl. *Science*, 287:1801–1804, 2000.

# Appendix A - Data Processing Code

This appendix contains an example of the data processing code written in Delphi to calculate the averages and standard deviations from the raw data obtained from an experiment. The example discussed was used to process raw data obtained from a variable temperature IV characteristics experiment. Figure 1 shows the graphic user interface for the program. The raw data obtained from the experiment was written sequentially to a file with the voltage, current and temperture of the current data point written to a line in the file, each value separated by a tab. All of the data for each of the temperatures invesigated were written to a single file. The program's job was to separate the data points for each temperature and average the ten data points taken at each voltage step. The program would also calculate the standard deviation from these ten data points. This was achieved by separating each data type: voltage, current and temperature into separate arrays which were each manipulated individually to obtain the desired results. Once the averages and standard deviations were calculated, the data taken at each different temperature had to be grouped together. The number of data points taken at each temperature was a known value and this was used to separate out the data at different temperatures. Finally each data set for each different temperature was loaded into a separate file with the sample name and average temperature written to the name of the file for identification purposes.

## Code

The code for the above graphical user interface is given below. Annotations to the code follow the special character //:

```
unit IV2_u;

{$mode objfpc}{$H+}
```

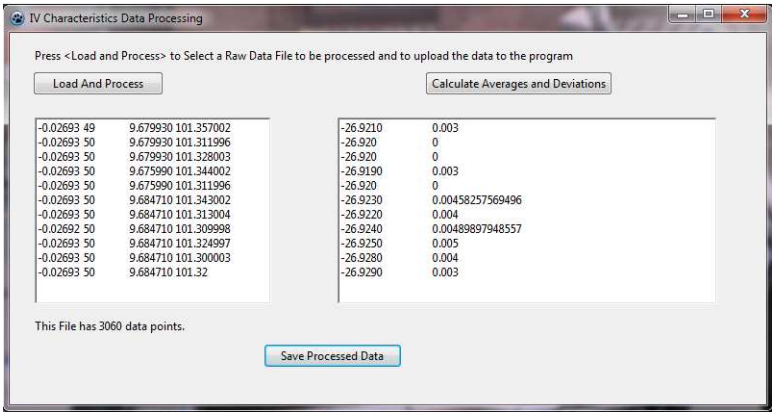


Figure 1: The graphical user interface for the program written to process the raw data obtained from a variable temperature IV characteristics experiment.

```
interface

uses
  Classes, SysUtils, FileUtil, Forms, Controls, Graphics, Dialogs, StdCtrls,
  RichMemo;

type

  { TfrmDataProcessing }

  TfrmDataProcessing = class(TForm)
    btnLoadandProcess: TButton;
    btnCalculate: TButton;
    btnSave: TButton;
    lblLoadInstructions: TLabel;
    lblNumberOfDataPoints: TLabel;
    odgRawDataFile: TOpenDialog;
    redArrayContents: TRichMemo;
    redAverages: TRichMemo;
    procedure btnCalculateClick(Sender: TObject);
    procedure btnLoadandProcessClick(Sender: TObject);
    procedure btnSaveClick(Sender: TObject);
  private
    { private declarations }
  public
    { public declarations }
```

```
  end;

  type //Declares the array data type required for the program
  TDataArray = array[1..10000] of real;

  const //Declares the constants used in the program
  TEMPNUMB = 510;
  VOLTNUMB = 10;
  CURRNUMB = 10;
  READNUMB = 51;

var //Declares the global variables used in the program
  frmDataProcessing: TfrmDataProcessing;
  iLineCounter, iAverageTempCount, iAverageVoltageCount,
  \\iAverageCurrentCount : integer;
  arrTemp, arrCurrent, arrVoltage, arrAverageTemp, arrAverageVoltage, \\
  arrDeviationVoltage,arrAverageCurrent, arrDeviationCurrent, arrDeviationTemp,
  \\ arrTemporary : TDataArray;

implementation

{$R *.lfm}

procedure CheckFileExists(var pFilePath : string); //Checks if the Chosen
\\File Exists (older operating systems)
begin
  if FileExists(pFilePath) <> true
    then
      begin
        MessageDlg('You Did Not Select a File or File does not Exist!',
        \\mtError, [mbOK], 0);
        Exit
      end;
end;

procedure ReadRawData(var pLineCounter : integer; var pFilePath : string;\\
var pRawData : TextFile; var parrTemp : TDataArray; var parrCurrent : \\
TDataArray; var parrVoltage : TDataArray); //Reads in Raw Data from the\\
 text file made by LabView and sorts it into separate arrays
```

```
var
  sTempString, sCurrentNumber : string;
  k, iNumberCount : integer;
begin
  sTempString := '' ;
  pLineCounter := 0;
  AssignFile(pRawData, pFilePath);
  Reset(pRawData);
  while NOT Eof(pRawData) do
    begin
      iNumberCount := 0;
      sCurrentNumber := '';
      Readln(pRawData, sTempString);
      Inc(pLineCounter);
      sTempString := sTempString + #9; //Adds a tab at the end of a line\\
       read in from the file so the last entry can be identified
      for k := 1 to Length(sTempString) do //Separates Numbers in the \\
       text file and sorts them into their arrays
        begin
          if sTempString[k] = #9
            then
              begin
                Inc(iNumberCount);
                Case iNumberCount of
                  1 : parrVoltage[pLineCounter] := \\
                   StrToFloat(sCurrentNumber);
                  2 : parrTemp[pLineCounter] := \\
                   StrToFloat(sCurrentNumber);
                  3 : parrCurrent[pLineCounter] := \\
                   StrToFloat(sCurrentNumber);
                end;
                sCurrentNumber:= '';
              end
            else
              begin
                sCurrentNumber := sCurrentNumber + sTempString[k];
              end;
        end;
    end;
```

```
end;

procedure CalculateAverageTemp(var parrTemp : TDataArray); //Calculates \\
 the average temperatures for each reading and the associated standard deviation
var
  k, iTemporary, j: integer;
  rAverage, rSum, rDevSum, rDifference, rSquared, rStandardDeviation : \\
   real;
begin
  iTemporary := 0;  //Counter for a temporary array of current values \\
   in average for use in standard deviation
  iAverageTempCount := 0;
  rSum := 0;
  rAverage := 0;
  for k := 1 to iLineCounter do
    begin
      Inc(iTemporary);
      rSum := rSum + parrTemp[k];
      arrTemporary[iTemporary] := parrTemp[k];
      if k Mod TEMPNUMB = 0
        then
          begin
            rAverage := rSum/TEMPNUMB;
            Inc(iAverageTempCount);
            rSum := 0;
            rDifference := 0;
            rSquared := 0;
            rDevSum := 0;
            arrAverageTemp[iAverageTempCount] := rAverage;
            for j := 1 to iTemporary do //Calculates the standard \\
             deviation
              begin
                rDifference := arrTemporary[j] - rAverage;
                rSquared := Sqr(rDifference);
                rDevSum := rDevSum + rSquared;
              end;
            rStandardDeviation := Sqrt((rDevSum/iTemporary));
            arrDeviationTemp[iAverageTempCount] := rStandardDeviation;
            iTemporary := 0;
```

```
          end;
    end;

end;

procedure CalculateAverageVoltage(var parrVoltage : TDataArray);
//Calculates the average voltage and associated standard deviation
var
  k, iTemporary, j: integer;
  rAverage, rSum, rDevSum, rDifference, rSquared, rStandardDeviation : \\
   real;
begin
  iTemporary := 0;
  iAverageVoltageCount := 0;
  rSum := 0;
  rAverage := 0;
  for k := 1 to iLineCounter do
    begin
      Inc(iTemporary);
      rSum := rSum + parrVoltage[k];
      arrTemporary[iTemporary] := parrVoltage[k];
      if k Mod VOLTNUMB = 0
        then
          begin
            rAverage := rSum/VOLTNUMB;
            Inc(iAverageVoltageCount);
            rSum := 0;
            rDifference := 0;
            rSquared := 0;
            rDevSum := 0;
            arrAverageVoltage[iAverageVoltageCount] := rAverage;
            for j := 1 to iTemporary do
              begin
                rDifference := arrTemporary[j] - rAverage;
                rSquared := Sqr(rDifference);
                rDevSum := rDevSum + rSquared;
              end;
            rStandardDeviation := Sqrt((rDevSum/iTemporary));
            arrDeviationVoltage[iAverageVoltageCount] := \\
```

```
              rStandardDeviation;
            iTemporary := 0;
          end;
    end;

end;

procedure CalculateAverageCurrent(var parrCurrent : TDataArray);
//Calculates the average current and the associated standard deviations
var
  k, iTemporary, j: integer;
  rAverage, rSum, rDevSum, rDifference, rSquared, rStandardDeviation \\
   : real;
begin
  iTemporary := 0;
  iAverageCurrentCount := 0;
  rSum := 0;
  rAverage := 0;
  for k := 1 to iLineCounter do
    begin
      Inc(iTemporary);
      rSum := rSum + parrCurrent[k];
      arrTemporary[iTemporary] := parrCurrent[k];
      if k Mod CURRNUMB = 0
        then
          begin
            rAverage := rSum/CURRNUMB;
            Inc(iAverageCurrentCount);
            rSum := 0;
            rDifference := 0;
            rSquared := 0;
            rDevSum := 0;
            arrAverageCurrent[iAverageCurrentCount] := rAverage * 1000;
            for j := 1 to iTemporary do
              begin
                rDifference := arrTemporary[j] - rAverage;
                rSquared := Sqr(rDifference);
                rDevSum := rDevSum + rSquared;
              end;
```

```
            rStandardDeviation := Sqrt((rDevSum/iTemporary));
            arrDeviationCurrent[iAverageCurrentCount] := \\
             rStandardDeviation * 1000;
            iTemporary := 0;
          end;
    end;
end;

{ TfrmDataProcessing }

procedure TfrmDataProcessing.btnLoadandProcessClick(Sender: TObject);
//Calls the procedures to check if the file exists and load the data \\
 into the program. The data is then displayed in the GUI
var
  RawData : TextFile;
  sFilePath, sAlter : string;
  l : integer;
begin
  if odgRawDataFile.Execute //Assigns a File path for the raw data file
    then
      sFilePath := odgRawDataFile.Filename;
  CheckFileExists(sFilePath);
  ReadRawData(iLineCounter, sFilePath, RawData, arrTemp, arrCurrent, \\
   arrVoltage);
For l := 1 to iLineCounter do
  begin
    if Length(FloatToStr(arrVoltage[l])) < 8
      then
        begin
          sAlter := FloatToStr(arrVoltage[l]);
          sAlter := sAlter + '0';
        end;
    redArrayContents.Lines.Add(FloatToStr(arrCurrent[l]) + #9 + sAlter \\
     + #9 + FloatToStr(arrTemp[l]));
  end;
lblNumberofDataPoints.Caption := 'This File has ' + \\
 IntToStr(iLineCounter) + ' data points.';
frmDataProcessing.Refresh;
```

```
end;

procedure TfrmDataProcessing.btnSaveClick(Sender: TObject);
//Writes the processed data to individual files for each temperature investigated
var
  sSampleName, sOneLine : string;
  WriteFile : TextFile;
  k, j, iEntryNumber : integer;
begin
  iEntryNumber := 1;
  sSampleName := InputBox('Sample Name', 'Please enter the name of the \\
   sample the entered data corresponds to', '');
  for k := 1 to iAverageTempCount do
    begin
      Assignfile(WriteFile, sSampleName + ' IV Characteristics at ' + \\
       FloatToStrF(arrAverageTemp[k], ffFixed, 5, 0) + 'K.txt');
      if FileExists(sSampleName + ' IV Characteristics at ' + \\
       FloatToStrF(arrAverageTemp[k], ffFixed, 5, 0) + 'K.txt') <> true
        then
          Rewrite(WriteFile)
        else
          Append(WriteFile);
      Writeln(WriteFile, FloatToStr(arrAverageTemp[k]) + #9 + \\
       FloatToStr(arrDeviationTemp[k]));
      for j := iEntryNumber to (iEntryNumber + 50) do
        begin
          Inc(iEntryNumber);
          sOneLine := FloatToSTr(arrAverageVoltage[j]) + #9 + \\
           FloatToSTr(arrDeviationVoltage[j]) + #9 + \\
            FloatToSTr(arrAverageCurrent[j]) + #9 + \\
             FloatToSTr(arrDeviationCurrent[j]);
          WriteLn(WriteFile, sOneLine);
        end;
      CloseFile(WriteFile);
    end;
end;

procedure TfrmDataProcessing.btnCalculateClick(Sender: TObject);
```

```
//Calls the procedures used to calculate the averages and standard \\
 deviations of the relavent quantities extracted from the raw data \\
  and displays them
var
  k : integer;
begin
  CalculateAverageTemp(arrTemp);
  CalculateAverageVoltage(arrVoltage);
  CalculateAverageCurrent(arrCurrent);
  redAverages.Lines.Add('Average Temperatures' + #9 + 'Standard Deviation');
  redAverages.Lines.Add('');
  for k := 1 to iAverageTempCount do
    redAverages.Lines.Add(FloatToStr(arrAverageTemp[k]) + #9 + #9 + \\
     FloatToStr(arrDeviationTemp[k]));
  redAverages.Lines.Add('');
  redAverages.Lines.Add('Average Voltages' + #9 + #9 + \\
   'Standard Deviation');
  redAverages.Lines.Add('');
  for k := 1 to iAverageVoltageCount do
    redAverages.Lines.Add(FloatToStr(arrAverageVoltage[k]) + '00' + \\
     #9 + #9 + FloatToStr(arrDeviationVoltage[k]));
  redAverages.Lines.Add('');
  redAverages.Lines.Add('Average Currents' + #9 + 'Standard Deviation');
  redAverages.Lines.Add('');
  for k := 1 to iAverageVoltageCount do
    redAverages.Lines.Add(FloatToStr(arrAverageCurrent[k]) + '0' + #9 \\
     + #9 + FloatToStr(arrDeviationCurrent[k]));
  frmDataProcessing.Refresh;

end;

end.
```

# Appendix B - LabView Automation Code

In order to automate the experiment and data collection process, software was written using the gaphical programming language LabView by National Instruments. LabView is specially designed to allow for easy interfacing with external measurement hardware such as oscilloscopes and scientific multimeters. The hardware was connected to the computer via diasy chaining general purpose interface bus (GPIB) cables which connected to a GPIB-USB adapter. Figure 2 shows the front panel of an example of the virtual instrument (VI) used to control the variable temperature resistance experiments. First the user must input the VISA assignments for the respective instruments connected to the computer. This is so that the VI sends the correct commands to the correct instruments. There are multiple instances for times when the same instrument is used more than once. The user must then choose the temperature range to be investigated and the file name for the data to be stored in.

The program controls the order in which events occur using a flat sequence. When the program is run the number of measurements to be made is determined from the temperature range inputed by the user. The program then activates the pump which controls the cryogen flow and sends the first set temperature to the temperature controller. This is so that the controller can maintain that temperature in the cryostat while the sample is cooling down and readings are being taken. The system is then set to wait for an hour. No events occur during this time. This period is to allow the sample to cool down and reach thermal equilibrium. Once the wait is over the program aquires the four probe resistance of the sample from the multimeter and the temperature of the sample from the temperature monitor. It takes ten readings, one every thirty seconds for five minutes to ensure that the average resistance and temperature can be calculated. Each of these data points is written to the file specified by the user. With this process completed the program begins its next itteration by decreasing the set temperature by 10 K and sending the new set temperature to the temperature controller. Once the entire temperature range has been explored the program concludes by shutting off the pump

and setting the set temperature to room temperature and writing it to the temperature controller. This is to warm the cryostat up so that the sample can be changed.

The block diagram containing the code was not included due to its large size.


Figure 2: The front panel of the virtual instrument created in LabView used to control the variable temperature resistance experiments.

# Appendix C - Intelligent Multiplexer Code

This appendix contains the code written to control the intelligent multiplexer. The code was written in a language based on Processing using the Arduino IDE. Figure 3 shows the graphical user interface for the Arduino IDE. Once written, the code (called a sketch) is uploaded to the ATMEL ATmega328 microprocessor loaded with the Arduino open source bootloader which controls the operation of the intelligent multiplexer.

The code is written so that the multiplexer can be in one of two modes: A mode (resistance wire configuration) and B mode (IV characteristic wire configuration). The mode the multiplexer is in determines how the wires are connected for a specific experiment. This is achieved by each mode changing the voltages sent to different sets of relays. When in B mode a number of other commands can be issued to the multiplexer. Commands can be sent to cause the voltage drop across the sample to be increased or decreased by different amounts. In the version of the code listed below, the voltage can be changed either by 7 mV or 500 mV

## Code

The code for the above graphical user interface is given below:

```
#include "SPI.h" // necessary library
int del=30; // used for various delays
word outputValue = 0; // a word is a 16-bit number
byte data = 0; // and a byte is an 8-bit number
int incomingByte = 0;
```

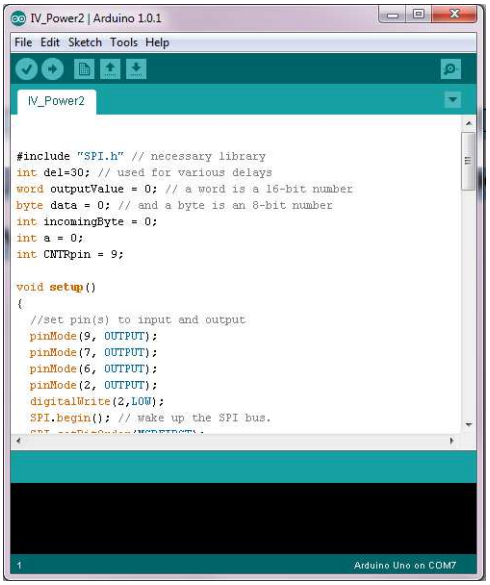


Figure 3: The graphical user interface for the Arduino IDE with some of the code for the intelligent multiplexer visable.

```
int a = 0;
int CNTRpin = 9;

void setup()
{
  //set pin(s) to input and output
  pinMode(9, OUTPUT);
  pinMode(7, OUTPUT);
  pinMode(6, OUTPUT);
  pinMode(2, OUTPUT);
  digitalWrite(2,LOW);
  SPI.begin(); // wake up the SPI bus.
  SPI.setBitOrder(MSBFIRST);
  Serial.begin(9600);
}

void loop()
{


  if (Serial.available() > 0) {
                // read the incoming byte:
```

```
incomingByte = Serial.read();
switch(incomingByte){
  case 52:
  if (a > 0){
  a = a - 1;
  }
  break;
  case 80:
  digitalWrite(2,HIGH);
  break;
  case 112:
  digitalWrite(2,LOW);
  break;
  case 53:
  a = 2048;
  break;
  case 48:
  a = 0;
  break;
  case 57:
  a = 4095;
  case 55:
  a = a + 66;
  break;
  case 51:
  a = a - 66;
  break;
  case 54:
  if (a < 4095){
  a = a + 1;
  }
  break;

  case 65:  //Case A (Resist mode)
  digitalWrite(7,HIGH);
  digitalWrite(6,HIGH);
  break;

  case 66: // Case B (IV Mode)
```

```
                digitalWrite(7,LOW);
                digitalWrite(6,LOW);
                break;

              }
              // say what you got:
              Serial.print("I received: ");
              Serial.println(a);
    }
    outputValue = a;
    digitalWrite(CNTRpin, LOW);
    data = highByte(outputValue);
    data = 0b00001111 & data;
    data = 0b00110000 | data;
    SPI.transfer(data);
    data = lowByte(outputValue);
    SPI.transfer(data);
    digitalWrite(CNTRpin,HIGH);


}
```